



Article (refereed) - postprint

Brannigan, Liam; Marshall, David P.; Naveira-Garabato, Alberto; Nurser, A.J.George. 2015

The seasonal cycle of submesoscale flows. *Ocean Modelling*.

[10.1016/j.ocemod.2015.05.002](https://doi.org/10.1016/j.ocemod.2015.05.002) (In Press)

© 2015 Elsevier B.V.

This version available at <http://nora.nerc.ac.uk/510885/>

NERC has developed NORA to enable users to access research outputs wholly or partially funded by NERC. Copyright and other rights for material on this site are retained by the rights owners. Users should read the terms and conditions of use of this material at

<http://nora.nerc.ac.uk/policies.html#access>

NOTICE: this is the author's version of a work that was accepted for publication in *Ocean Modelling*. Changes resulting from the publishing process, such as peer review, editing, corrections, structural formatting, and other quality control mechanisms may not be reflected in this document. Changes may have been made to this work since it was submitted for publication. A definitive version will be published in *Ocean Modelling*.

[10.1016/j.ocemod.2015.05.002](https://doi.org/10.1016/j.ocemod.2015.05.002) (

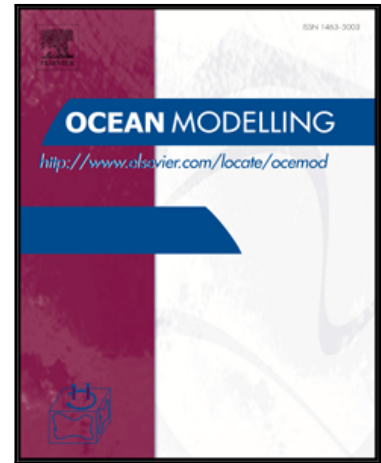
Contact NOC NORA team at
publications@noc.soton.ac.uk

Accepted Manuscript

The seasonal cycle of submesoscale flows

Liam Brannigan, David P. Marshall, Alberto Naveira-Garabato,
A.J.George Nurser

PII: S1463-5003(15)00080-3
DOI: [10.1016/j.ocemod.2015.05.002](https://doi.org/10.1016/j.ocemod.2015.05.002)
Reference: OCEMOD 974



To appear in: *Ocean Modelling*

Received date: 9 December 2014
Revised date: 21 April 2015
Accepted date: 4 May 2015

Please cite this article as: Liam Brannigan, David P. Marshall, Alberto Naveira-Garabato, A.J.George Nurser, The seasonal cycle of submesoscale flows, *Ocean Modelling* (2015), doi: [10.1016/j.ocemod.2015.05.002](https://doi.org/10.1016/j.ocemod.2015.05.002)

This is a PDF file of an unedited manuscript that has been accepted for publication. As a service to our customers we are providing this early version of the manuscript. The manuscript will undergo copyediting, typesetting, and review of the resulting proof before it is published in its final form. Please note that during the production process errors may be discovered which could affect the content, and all legal disclaimers that apply to the journal pertain.

Highlights

- Submesoscale-permitting simulations in an open ocean domain through the annual cycle are described.
- The surface spectral slopes vary through the year as the mixed layer depth changes.
- A large proportion of the mixed layer is subject to conditions of negative PV in winter both at fronts and inside mesoscale vortices.

ACCEPTED MANUSCRIPT

The seasonal cycle of submesoscale flows

Liam Brannigan^{a,*}, David P. Marshall^a, Alberto Naveira-Garabato^b, A.J. George Nurser^c

^a*Atmospheric, Oceanic & Planetary Physics, Clarendon Lab, University of Oxford, Oxford, England*

^b*University of Southampton, National Oceanography Center, Southampton, England*

^c*National Oceanography Center, Southampton, England*

Abstract

The seasonal cycle of submesoscale flows in the upper ocean is investigated in an idealised model domain analogous to mid-latitude open ocean regions. Submesoscale processes become much stronger as the resolution is increased, though with limited evidence for convergence of the solutions. Frontogenetical processes increase horizontal buoyancy gradients when the mixed layer is shallow in summer, while overturning instabilities weaken the horizontal buoyancy gradients as the mixed layer deepens in winter. The horizontal wavenumber spectral slopes of surface temperature and velocity are steep in summer and then shallow in winter. This is consistent with stronger mixed layer instabilities developing as the mixed layer deepens and energising the submesoscale. The degree of geostrophic balance falls as the resolution is made finer, with evidence for stronger non-linear and high-frequency processes becoming more important as the mixed layer deepens. Ekman buoyancy fluxes can be much stronger than surface cooling and are locally dominant in setting the stratification and the potential vorticity at fronts, particularly in the early winter. Up to 30% of the mixed layer volume in winter has negative potential vorticity and symmetric instability is predicted inside mesoscale eddies as well as in the frontal regions outside of the vortices.

Keywords: Submesoscale, mixed layer fronts, frontogenesis, symmetric instability, baroclinic instability, seasonal cycle, Ekman buoyancy flux

1. Introduction

1 The upper ocean stratification is an important control on the transfer of
 2 momentum and tracers between the atmosphere and ocean interior. The de-
 3 velopment of upper ocean stratification has historically been viewed as a one-
 4 dimensional process driven by surface buoyancy and frictional fluxes, with al-
 5 lowance for shear-driven mixing at the base of the mixed layer. These ideas are
 6

*Corresponding author: brannigan@atm.ox.ac.uk; +44 1865 282429

7 encapsulated in a number of one-dimensional parameterisation schemes for the
8 surface boundary layer (e.g. Price et al., 1986; Large et al., 1994). Attention
9 has since focused on the role a number of other processes play in setting up-
10 per ocean stratification such as geostrophic adjustment (Tandon and Garrett,
11 1994; Dale et al., 2008), frontogenesis (Hoskins and Bretherton, 1972; Lapeyre
12 et al., 2006; Shakespeare and Taylor, 2013; Gula et al., 2014), surface waves and
13 Langmuir turbulence (Grant and Belcher, 2009; Belcher et al., 2012; McWilliams
14 and Fox-Kemper, 2013; Hamlington et al., 2014; Sutherland et al., 2014; Haney
15 et al., Subm. to JPO), Ekman buoyancy fluxes (hereafter EBF, Thomas, 2005;
16 Mahadevan, 2006; Thomas and Ferrari, 2008; Thomas et al., 2013), symmetric
17 and inertial instabilities (Haine and Marshall, 1998; Thomas and Taylor, 2010;
18 D’Asaro et al., 2011; Thomas et al., 2013; Thomsen et al., 2013; Bachman and
19 Taylor, 2014), and mixed layer baroclinic instabilities (Samelson, 1993; Nurser
20 and Zhang, 2000; Boccaletti et al., 2007; Mahadevan et al., 2010; Skillingstad
21 and Samelson, 2012; Bachman and Fox-Kemper, 2013; Brüggemann and Eden,
22 2014) amongst others. While there is evidence for each of these processes affect-
23 ing upper ocean stratification, the interactions between them and their relative
24 strength over the seasonal cycle remain major outstanding questions (Capet
25 et al., 2008a; Lévy et al., 2010; Taylor and Ferrari, 2010; Belcher et al., 2012;
26 Haney et al., 2012; Mensa et al., 2013; Hamlington et al., 2014; Callies et al.,
27 2015).

28 An important point of reference for this work is an insightful series of papers
29 by Capet and co-authors (Capet et al., 2008a,b,c), that examine the transition
30 from mesoscale to submesoscale dynamics in a model domain analogous to the
31 California Current System. An advantage of this approach over a channel model
32 configuration is that the submesoscale processes occur in the context of the
33 strain induced by a larger scale eddy field. This strain may be an important
34 control on the growth rate of instabilities (Bishop, 1993; Spall, 1997; McWilliams
35 and Molemaker, 2011; Thomas, 2012). A comparable experimental methodology
36 is employed in this work whereby simulations are run over a resolution range
37 from mesoscale-resolving to submesoscale-permitting. These simulations depart
38 from previous works in a number of ways. Firstly, a seasonally varying surface
39 buoyancy forcing is employed and so the mean mixed layer depth varies by
40 an order of magnitude through the year. Secondly, no temperature-restoring
41 is used and so the model stratification can diverge as the resolution becomes
42 finer. Thirdly, the domain used here is analogous to an open ocean region rather
43 than an eastern boundary current region (Capet et al., 2008a,b,c) or a western
44 boundary current region (Mensa et al., 2013; Gula et al., 2014).

45 This experiment is carried out in an idealised configuration intended to be
46 analogous to the OSMOSIS (Ocean Surface Mixing - Ocean Submesoscale Inter-
47 action Study) observation site in the North Atlantic. The observation site is the
48 Porcupine Abyssal Plain located near (16°W , 49°N) a region where mean flows
49 are weak and mesoscale eddies dominate the kinetic energy budget (Painter
50 et al., 2010). This numerical experiment complements a moored array of instru-
51 ments, seaglider deployments and two process cruises in the project. Compar-
52 isons will be made to these observations as the results are presented, though we

53 note the model has not been ‘tuned’ to replicate the observations.

54 This manuscript is structured as follows. The experimental set-up is given in
 55 Section 2. The structure of the buoyancy and velocity fields and the balance re-
 56 lationships that connect them are described in Section 3. The magnitude of the
 57 different submesoscale processes across the seasonal cycle in Section 4. A sum-
 58 mary and discussion of the implications for efforts to observe and parameterise
 59 submesoscale flows follow in Section 5.

60 2. Experimental set-up

61 2.1. Model domain

62 The simulations are integrated using the MITgcm (Marshall et al., 1997) in
 63 a hydrostatic configuration. The model set-up is analogous to the OSMOSIS
 64 observation area at the Porcupine Abyssal Plain site. As such, the configuration
 65 is that of an open ocean location in the mid-latitudes where the kinetic energy
 66 budget is dominated by mesoscale eddies. The domain is doubly-periodic with
 67 side-length of 256 km. The bottom boundary is at 3,700 m depth and the model
 68 domain is spanned with 200 vertical levels. The vertical grid-spacing is reduced
 69 near the top and bottom boundaries to 3 m to better resolve the boundary
 70 layer processes of interest and increases gradually to a maximum of 32.5 m in
 71 the interior.

72 A series of simulations are carried out with uniform horizontal grid resolu-
 73 tions of 4 km, 2 km, 1 km and 0.5 km. The 4 km run acts as the control for our
 74 experiment, though comparisons are also made with observations to ensure the
 75 model state is a reasonable representation of the real ocean. The simulations
 76 are run on the UK ARCHER supercomputer, a Cray XC30 system. All of the
 77 runs are integrated for at least five years with the fifth year used to perform the
 78 analysis.

79 2.2. Numerical configuration

80 A linear equation of state in temperature is employed with a thermal expan-
 81 sion coefficient $\alpha = 2 \times 10^{-4} \text{ K}^{-1}$ and so $b = g\alpha(T - T_{ref})$ where b is buoyancy,
 82 $g = 9.81 \text{ m s}^{-2}$ is gravity, T is temperature and T_{ref} is a reference temper-
 83 ature. Simulations of geostrophic turbulence generate a downscale cascade of
 84 enstrophy that must be dissipated to prevent it accumulating at the grid-scale.
 85 Enstrophy is also dissipated in the momentum equation using adaptive viscous
 86 schemes first developed by Smagorinsky (1963), Leith (1996) and Fox-Kemper
 87 and Menemenlis (2013). Recent results show that adaptive viscous schemes
 88 are necessary to allow submesoscale turbulence to develop (Ilicak et al., 2012;
 89 Graham and Ringler, 2013; Ramachandran et al., 2013). Diffusion is applied to
 90 horizontal gradients in temperature. For both horizontal diffusion and viscosity,
 91 biharmonic operators are chosen over Laplacian operators so that explicit dif-
 92 fusion and viscosity are targeted at the highest wavenumbers (e.g. Griffies and
 93 Hallberg, 2000; Graham and Ringler, 2013). At all resolutions the Smagorinsky

94 coefficient is 3, while the Leith and modified Leith coefficients are 1. The bi-
 95 harmonic temperature diffusion coefficient is $4 \times 10^7 \text{ m}^4 \text{ s}^{-1}$ at 4 km resolution
 96 and reduced by a factor of four for each doubling in resolution. A partial-slip
 97 bottom boundary condition is imposed with a quadratic bottom drag (Arbic
 98 and Scott, 2008) using a non-dimensional quadratic drag coefficient of 3×10^{-3} .

99 In addition, vertical mixing of both heat and momentum is carried out with a
 100 Laplacian operator with a constant diffusion coefficient of $4 \times 10^{-5} \text{ m}^2 \text{ s}^{-1}$. The
 101 mixed layer depth is defined throughout as the first depth where the temperature
 102 difference from the surface is greater than 0.1° C .

103 The advection of temperature is carried out using the Prather scheme (Prather,
 104 1986). This is an upwind scheme that conserves second-order moments in sub-
 105 grid tracer distributions and so helps to preserve the sharp frontal structures
 106 of interest. Hill et al. (2012) show that the effective diffusivity of the Prather
 107 scheme is similar to the level of diffusion estimated for the real ocean by tracer
 108 release studies. The model's default second-order centered advection scheme is
 109 employed for momentum.

110 The timestep is 400 s at 4 km resolution and is then reduced by a factor of
 111 two with each doubling in resolution. The model is integrated on an f -plane
 112 with a Coriolis frequency $f = 10^{-4} \text{ s}^{-1}$. Note that no temperature relaxation
 113 conditions are employed and so the model solution can evolve freely.

114 2.3. Boundary layer parameterisation

115 In the vertical, the model is run with the K -profile parameterisation (KPP ,
 116 Large et al. (1994)) for the surface boundary layer. This scheme is in prac-
 117 tice a suite of parameterisations that aim to represent a number of mixed layer
 118 processes. The KPP scheme increases the vertical viscous/diffusive coefficients
 119 (hereafter 'diffusive coefficients') based on the surface wind stress. It also in-
 120 creases the diffusive coefficients if there is elevated shear at the base of the mixed
 121 layer based on a Richardson number criteria. In the event of destabilising sur-
 122 face buoyancy forcing the KPP scheme introduces a vertical non-local transport
 123 to capture the effect of vertical convective mixing (Marshall and Schott, 1999).
 124 The KPP scheme also applies higher diffusive coefficients in the event of negative
 125 stratification, even if this is not associated with destabilising surface buoyancy
 126 forcing as can occur in the presence of down-front winds. In these cases of static
 127 instability the KPP scheme applies a high ($5 \times 10^{-3} \text{ m}^2 \text{ s}^{-1}$) vertical diffusion
 128 coefficient rather than instantaneously mixing buoyancy as done by the default
 129 MITgcm convective adjustment scheme or the Price et al. (1986) scheme.

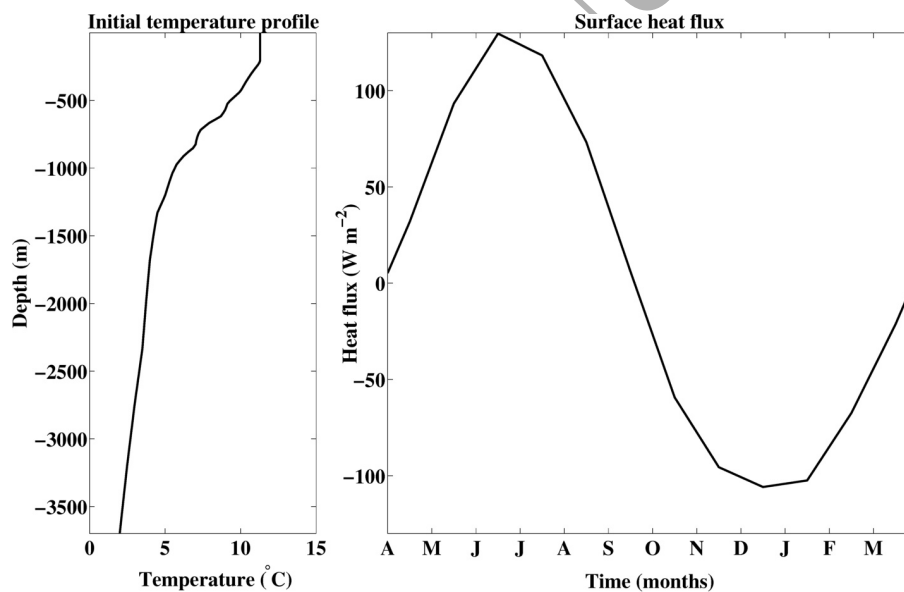
130 2.4. Initial and boundary conditions

131 The model is initialised at rest with a horizontally uniform temperature
 132 profile. The initial vertical temperature profile (Figure 1, left panel) is derived
 133 from an Argo float near the Porcupine Abyssal Plain observation site. This
 134 profile was sampled on 23rd March 2012 and is selected as a temperature profile
 135 with minimal signs of internal wave heaving or instrument noise.

136 The model is forced at the surface by a heat flux and wind forcing. The pre-
 137 scribed heat flux is uniform across the domain and averages to zero over each

138 360-day year (Fig. 1, right panel) with values based on the sum of the net short-
 139 wave, longwave, sensible and latent heat fluxes from the monthly climatology
 140 of Berry and Kent (2009) for the Porcupine Abyssal Plain observation region.
 141 These heat fluxes are applied to the uppermost model level. As such, heating
 142 fluxes result in a more rapid restratification than in the real ocean where short-
 143 wave radiative fluxes penetrate in an exponentially decaying manner through
 144 the water column. The experiment aims to understand the response of mixed
 145 layer dynamics to the seasonal cycle in buoyancy forcing. Higher frequency
 146 variability, including diurnal effects, are not included in the main experiments
 147 described here.

148 References are made to ‘summer’ and ‘winter’ as shorthand for the periods
 149 of heating and cooling respectively. The model integration begins with strati-
 150 fication derived from late March conditions – as such the heating period is the
 151 first half of every model year and the cooling period is the second half. To aid
 152 readability and comparisons with observations from the real ocean, the model
 153 outputs are equated with the month they correspond to from the buoyancy
 forcing.



154 Figure 1: (Left panel) The initial temperature profile for all simulations. (Right panel) The
 155 heat flux into the domain through the year. The model ‘summer’ is the first half of the year
 and the model ‘winter’ is the second half.

156 While the surface heat flux creates an annual cycle in stratification and
 157 mixed layer depth, the wind forcing produces a field of geostrophic turbulence
 158 and an Ekman transport in the near-surface. The forcing scheme used is based
 159 on that of Koszalka et al. (2009) with a streamfunction (ψ) to generate the
 wind stress that varies in space and time. The consequent curl of the wind

160 stress causes isopycnals to tilt locally through Ekman pumping or suction. The
 161 velocity field undergoes Rossby adjustment to the tilt of the isopycnals and the
 162 non-linear eddy interactions then induce a turbulent eddy field.

163 The streamfunction is constructed using zonal and meridional Fourier modes,
 164 an example of which can be seen in Figure 2. Unlike Koszalka et al. (2009),
 165 where a random component to each streamfunction is introduced in Fourier
 166 space, a random phase is added onto each streamfunction component-pair in
 167 order to randomise the spatial structure of the forcing from month to month
 168 with:

$$\psi = \psi_0 \sum_{k,l=1}^3 \sin(kx + \phi_1(k,l)) \sin(ly + \phi_2(k,l)), \quad (2.1)$$

169 where $\psi_0 = 0.02 \text{ N m}^{-1}$, x and y are the zonal and meridional coordinates
 170 respectively, k and l are the zonal and meridional domain wavenumbers respec-
 171 tively, and ϕ_i is a random phase. A new streamfunction is generated each month
 172 and the model linearly interpolates between the successive streamfunctions to
 173 give a wind field that varies smoothly in time. Inspection of the results show
 174 this gives rise to a small amplitude monthly cycle that is not readily appar-
 175 ent in the key model outputs in the presence of the generally turbulent flow.
 176 The streamfunction for wind forcing is produced for the 4 km run and then
 177 interpolated to the finer resolution grids.

178 In addition, a constant zonal wind of 0.05 N m^{-2} is added to ensure the mixed
 179 layer depth extends beyond the uppermost model layer during periods of stabil-
 180 ising heat forcing such that the vector wind stress $\tau = 0.05\mathbf{i} + \mathbf{k} \times \nabla\psi$
 181 where \mathbf{i} is the zonal unit vector and \mathbf{k} is the vertical unit vector. The constant
 182 zonal wind is about five times larger than the root-mean-square magnitude of
 183 the spatially-varying wind derived from the streamfunction in equation (2.1),
 184 and so it is the main driver of the Ekman transport.

185 The wind forcing has length scales of 20 - 256 km and so is shorter than
 186 the atmospheric length scales with the greatest energy in the mid-latitudes
 187 (Nastrom and Gage, 1985). However, the length scales of the forcing are still
 188 comparable to the baroclinic deformation radius of approximately 40 km. A test
 189 experiment has been carried out with a wind streamfunction that was constant
 190 in time. Analysis of this run after one year showed no imprint of the wind-forcing
 191 in the model output. This provides confidence that the non-linear dynamics of
 192 the eddy field dominate the solution, rather than the detailed structure of the
 193 wind forcing. The wind forcing in this experiment is continuous, but weak, with
 194 a magnitude about one-third of the root-mean-square wind stress magnitude
 195 estimated from the ERA-interim re-analysis for the region.

196 2.5. Averaging operator

The averaging operator denoted by an overbar is a horizontal average over
 a model level:

$$\overline{g(\mathbf{x}, t)} = \frac{1}{A} \int_x \int_y g dx dy, \quad (2.2)$$

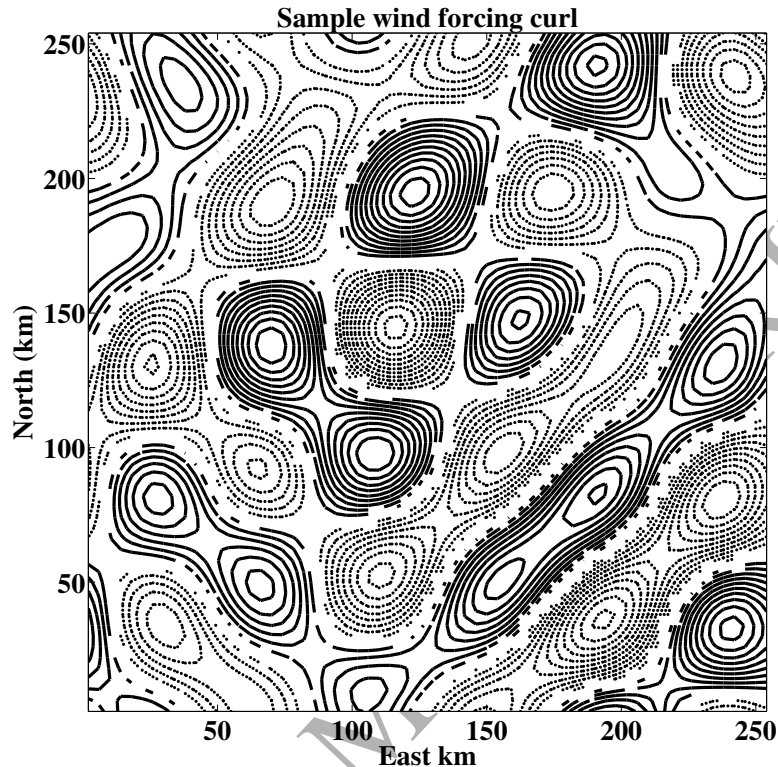


Figure 2: A snapshot of the wind-forcing used in the model for one month, presented as the curl of the streamfunction. Solid lines are positive contours and dotted lines are negative contours with intervals of 10^{-7} m s^{-2} .

197 where g is an arbitrary function, \mathbf{x} is the position vector, t is time and A is the
198 horizontal area.

199 3. Results

200 The overall buoyancy and momentum fields are compared at different reso-
201 lutions in the spin-up phase and throughout the seasonal cycle.

202 3.1. Spin-up and inter-annual variability

203 At the outset of the runs, the solutions are similar across the range of reso-
204 lutions (Figure 3, all panels). The solutions begin to diverge between resolutions
205 after about 120 days both in terms of the standard deviation of sea surface tem-
206 perature (SST) anomalies, the mean mixed layer depth and the mean kinetic
207 energy at the surface (Fig. 3, upper three panels). The mean energy input from
208 the wind is similar at all resolutions (Fig. 3, bottom panel). The wind energy

209 input is similar across resolutions despite the higher surface kinetic energy at
 210 finer resolution as the largest kinetic energy is found in the mesoscale vortices,
 211 where the wind is aligned with the flow on one side of the vortex but opposed
 212 to the flow on the other side, and so the energy input largely cancels out. From
 213 the third year of the simulations the differences between the years are in the
 214 range of year-to-year variability (Fig. 3, upper three panels). Fields with greater
 inter-annual variability are noted in the results below.

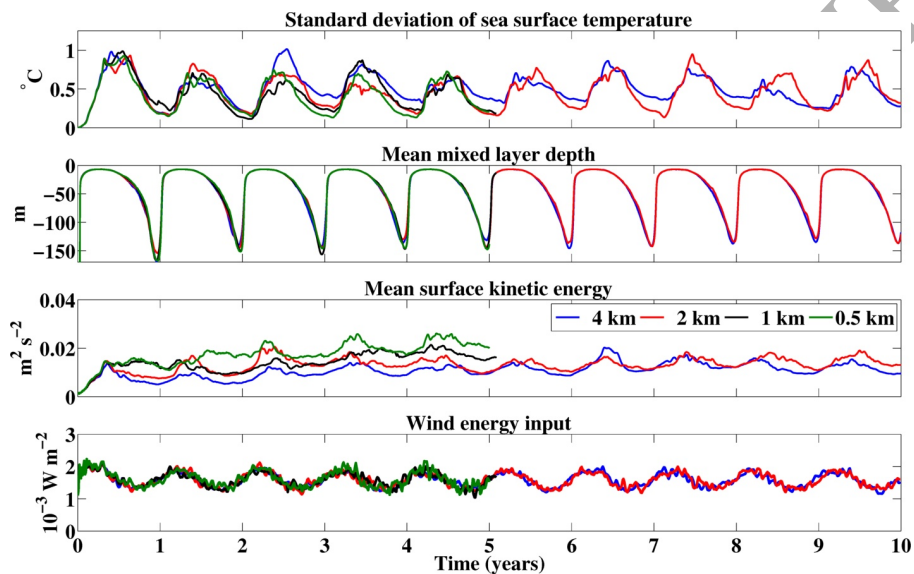


Figure 3: Model fields during spin-up. (Top row) Standard deviation of sea surface temperature. (Second row) The mean mixed layer depth. (Third row) Mean kinetic energy at the surface. (Bottom row) The mean input of kinetic energy by the wind stress $\tau \cdot \mathbf{u}$. The two coarser resolution simulations have been run for a further five years to Year 10.

215

216 3.2. Vertical and horizontal buoyancy distributions

217 Level mean vertical temperature profiles (\bar{T}) at the end of the heating and
 218 cooling period are shown in Figure 4 below. These profiles show that at finer
 219 resolution there is a cooler and deeper mixed layer (Fig. 3, second row) and
 220 this is found in both summer and winter. The dynamical causes of this will
 221 be explored further in a subsequent manuscript. The difference in \bar{T} between
 222 the runs falls to zero by 350 m depth. The range of mixed layer depths from
 223 approximately 0 m to 250 m in the model is similar to those estimated over the
 224 seasonal cycle from seaglider observations at the Porcupine Abyssal Plain site
 225 (Damerell et al., in prep. for Geophys.Res.Lett.).

226 Qualitative differences in the horizontal distribution of buoyancy are illus-
 227 trated in the snapshots of the magnitude of buoyancy gradients at the sea surface

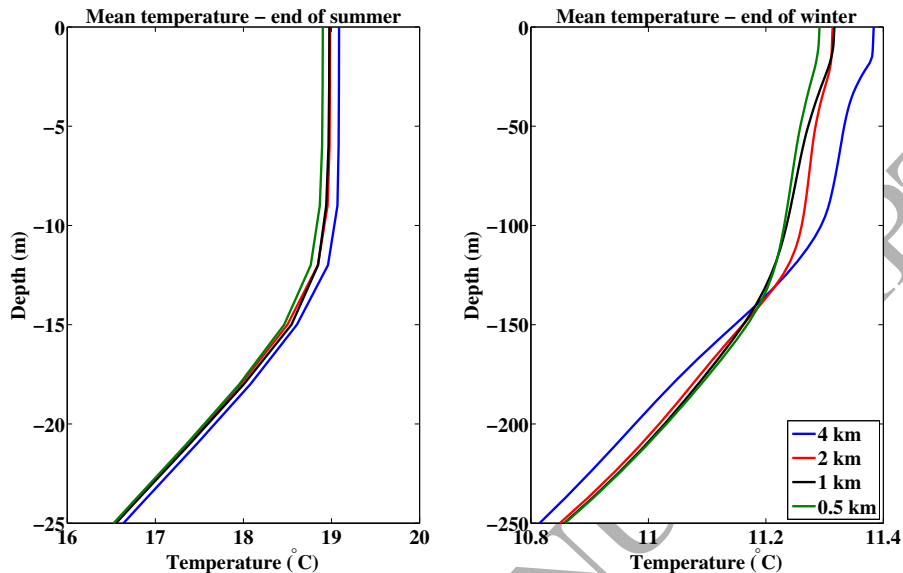


Figure 4: Mean temperature profiles. (Left panel) The temperature profile at the end of summer in the fifth model year. (Right panel) The temperature profile at the end of winter in the fifth model year. Note the different scales between the panels on both axes.

228 in Fig. 5. These snapshots are from January of the fifth year of the simulations,
 229 when the mean mixed layer depth is approximately 90 m. Fig. 5 shows that
 230 fronts become stronger, sharper and more sinuous as the resolution is made
 231 finer. In contrast to Capet et al. (2008a), filamentary submesoscale features are
 232 also present inside the large vortices, for example in the anti-cyclone at (50 km,
 233 50 km) in the lower-right panel of Fig. 5. This filamentation occurs whenever
 234 the mixed layer is deeper than approximately 40 m at the finest resolution.

235 Values of $|\overline{\nabla_h b}|$, the level-mean magnitude of the horizontal buoyancy gra-
 236 dient, where ∇_h is the horizontal gradient operator, are shown in Fig. 6. The
 237 root-mean-square magnitude of these gradients is $O(10^{-7} \text{ s}^{-2})$, with the largest
 238 values an order of magnitude stronger, typical of those observed in the mid-
 239 latitude mixed layer (e.g. Hosegood et al., 2006). There is an increase in $|\overline{\nabla_h b}|$
 240 as the resolution is made finer, as previously noted by Capet et al. (2008a).
 241 At the start of the heating period – for example in May in Fig. 6 – the mean
 242 gradients are low at all resolutions. As the heating period progresses $|\overline{\nabla_h b}|$ in-
 243 creases more quickly as the resolution is made finer, for example in July in Fig.
 244 6. It then decreases more rapidly at finer resolution in the cooling period as
 245 the mixed layer begins to deepen. We note that there is significant variation
 246 in the values of $|\overline{\nabla_h b}|$ from year-to-year, though the annual cycle persists. The
 247 seasonal cycle in horizontal buoyancy gradients found here agrees with glider
 248 observations from the Porcupine Abyssal Plain site. Alternative model forcings

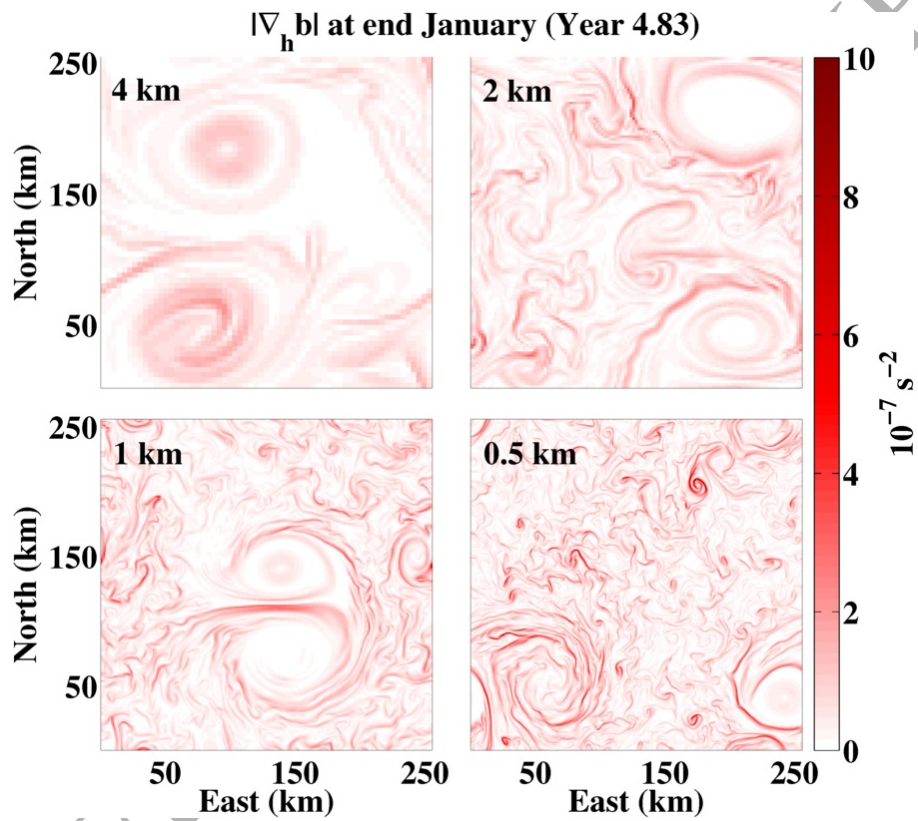


Figure 5: A snapshot of the magnitude of the sea surface buoyancy gradient at the indicated grid resolutions. The snapshots are derived from the model state in late January (year 4.83) when the mean mixed layer is approximately 90 m deep.

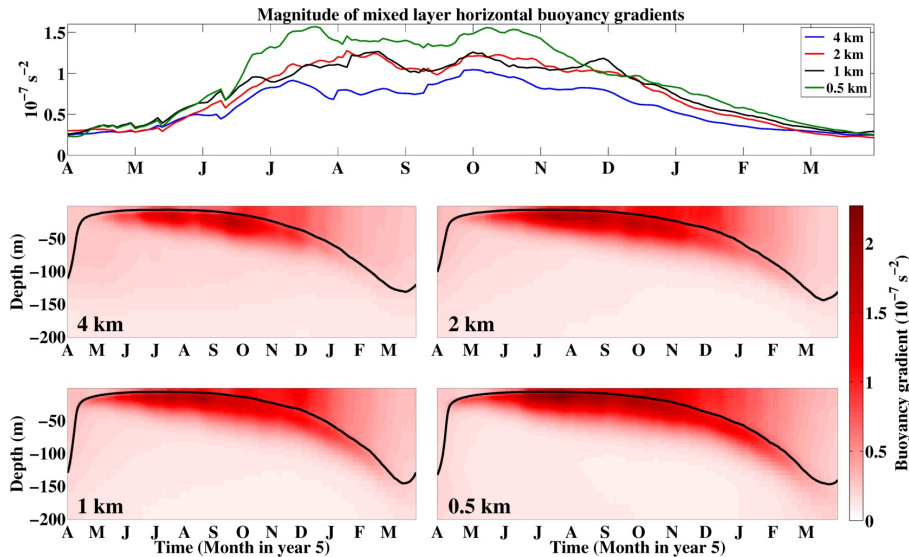


Figure 6: The mean horizontal buoyancy gradient $|\overline{\nabla_h b}|$ over the fifth year of the simulations at 2-day intervals. (Upper panel) The mean horizontal buoyancy gradient in the mixed layer. (Lower panels) The vertical profile of $|\overline{\nabla_h b}|$. The black line in the lower panels shows the mean mixed layer depth at that time.

249 that include a diurnal cycle in heating and stronger wind forcing have been
 250 carried out at 2 km resolution. The results of these experiments have a similar
 251 seasonal cycle of horizontal buoyancy gradients.

252 While $|\overline{\nabla_h b}|$ captures variability at the grid scale, the horizontal distribution
 253 of buoyancy over the whole surface level can be considered using the power spec-
 254 tral density (PSD) of SST. The spectra are calculated in horizontal wavenumber
 255 shells after the application of a 2D Hanning window. As for Capet et al. (2008c)
 256 the spectra are multiplied by four to recover the variance from before the win-
 257 dowing operation. Figure 7 shows the spectra averaged over April to September
 258 (left panel) and October to March (right panel). There is an increase in vari-
 259 ability at shorter wavelengths as the resolution is made finer, previously found
 260 by Capet et al. (2008a). A comparison of the upper panels in Fig. 7 shows that
 261 there is a shallowing of the spectral slope from summer to winter.

262 3.3. Velocity field

263 The root-mean-square velocities are about 15 cm s^{-1} at fine resolution, that
 264 is about 30% less than those observed at the observation site (Painter et al.,
 265 2010). The mean flow in the model is an Ekman spiral driven by the zonal mean
 266 wind stress (not shown).

267 The slopes of the power spectral density of surface velocity are similar to
 268 those for SST anomalies with the slope shallowing from near -3 in summer (Fig-

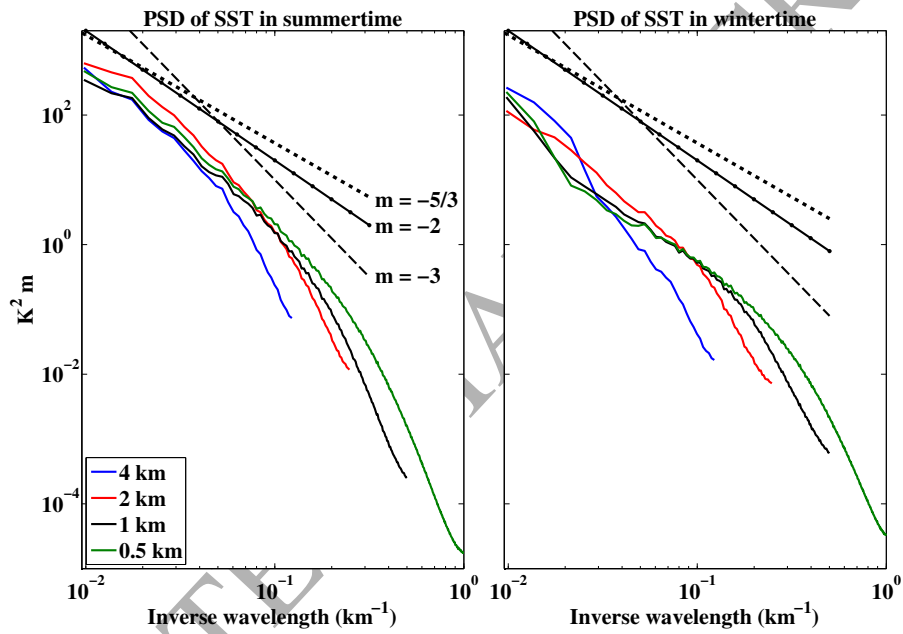


Figure 7: The power spectral density of sea surface temperature. (Left panel) The horizontal spectra averaged over the heating period. (Right panel) The horizontal spectra averaged over the cooling period. The dotted lines show reference slopes m in log-log space.

269 ure 8, upper-left panel) to approximately -2 as the winter progresses (Figure 8,
 270 upper-right panel). The slope is evaluated quantitatively by performing a linear
 271 regression on the power spectral density in log-log space at each resolution over
 272 the annual cycle. To reduce domain-scale and grid-scale effects, this regression
 273 is carried out over the range of wavelengths from four times the grid spacing
 274 for each simulation to 100 km. The regressed slope remains merely an estimate
 275 of the change in the spectral slope due to increasing curvature in the slope in
 276 winter. The time series of regressed slopes in Fig. 8 (lower panel) shows that the
 277 slope quickly steepens to values between -4 and -3 in the restratification period
 278 (April to May). The slope remains relatively steep until the cooling begins in
 279 September, at which point the slope starts shallowing until reaching a value be-
 280 tween $-5/3$ and -2 in December when the mixed layer has reached approximately
 281 40 m depth. The slope then stops shallowing even as the mixed layer continues
 282 to deepen to 150 m in March. These seasonal variations in slopes are consis-
 283 tent with observations of the North Atlantic (Callies et al., 2015) and numerical
 284 simulations of the North Atlantic that resolve basin-scale features (Lévy et al.,
 285 2010; Mensa et al., 2013). We note that the steeper slopes in summer could
 286 also be due to the mixed layer deformation radius with shallow mixed layers
 287 being less than the model grid resolution. The seasonal cycle in the slope shown
 288 in Fig. 8 (lower panel) occurs consistently from year-to-year in the three finer
 289 resolution cases. The coarsest resolution case is more variable, but the same
 290 overall cycle emerges if a multi-year average of the cycle is taken.

291 Figure 9 (left panel) shows the vertical profile of the power spectral density of
 292 the horizontal velocity in January at the finest resolution. The plot is a colour
 293 equivalent of the spectra in Fig. 8 (upper panels). Shallower spectral slopes
 294 are found where the light colours extend to shorter wavelengths. Fig. 9 (right
 295 panel) shows the same regression slopes as Fig. 8 (lower panel), but applied in
 296 the vertical. The regime of shallow spectral slopes is confined to the mixed layer
 297 at all resolutions, the mean depth of which is marked by a horizontal line of the
 298 same colour. We note that the transition from shallow to steep slopes happens
 299 near the mean mixed layer depth of 60 m in Fig. 9, and so is not related to the
 300 increase in vertical grid spacing that begins from 90 m depth at all resolutions.
 301 These vertical profiles of spectral slopes are consistent with the mixed layer
 302 being better approximated by quasi-geostrophic dynamics with a vertical scale
 303 of the mixed layer depth rather than surface quasi-geostrophy (sQG), as in the
 304 latter case shallower spectral slopes are also expected below the mixed layer
 305 (Callies and Ferrari, 2013).

306 The implications of the seasonal cycle in the power spectral density of sur-
 307 face velocity at the different resolutions is apparent in relative vorticity at the
 308 surface through the year. The embedded animation in Figure 10 shows that
 309 the steep spectral slopes in summer correspond to a vorticity field dominated
 310 by the largest mesoscale vortices. As the cooling begins from September, more
 311 submesoscale features in relative vorticity emerge in frontal regions and inside
 312 the anti-cyclonic eddies. As the winter progresses these come to occupy the
 313 entire domain.

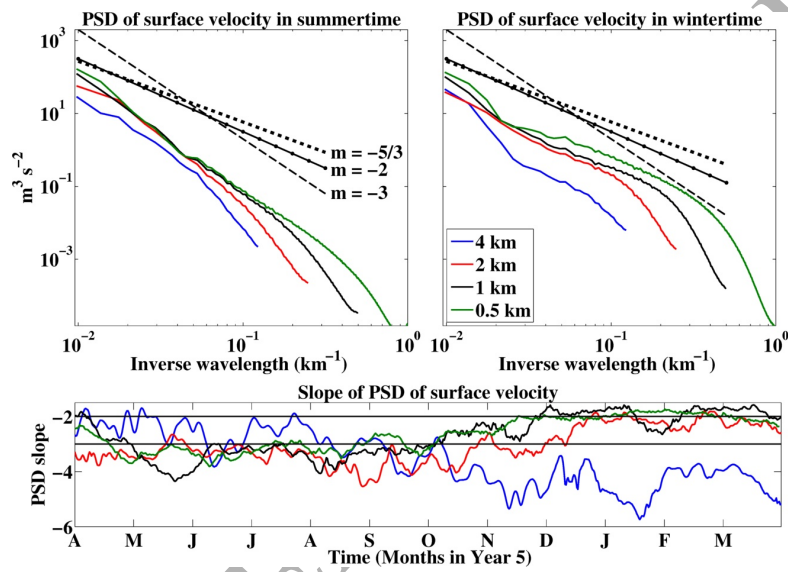


Figure 8: The power spectral density for surface velocity. (Upper-left panel) The power spectral density averaged over the heating period (April - September). (Upper-right panel) The power spectral density averaged over the cooling period (October - March). The dotted lines show reference slopes m in log-log space. (Lower panel) Time series of the regressed spectral slopes. The reference horizontal lines in the lower panel are at -2 and -3. The upper-limit on the y-axis is a slope of -5/3.

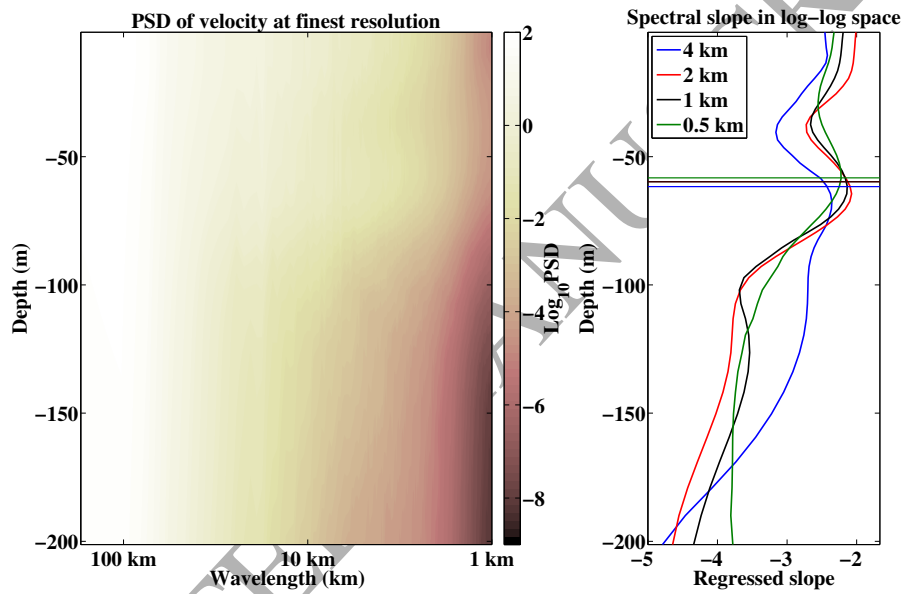


Figure 9: The vertical structure of the power spectral density of velocity in early January during the cooling phase. (Left panel) A color plot of the PSD at fine resolution. (Right panel) The spectral slope for all resolutions as estimated from a linear regression in log-log space. The coloured horizontal lines show the mean mixed layer depth at the corresponding resolution.

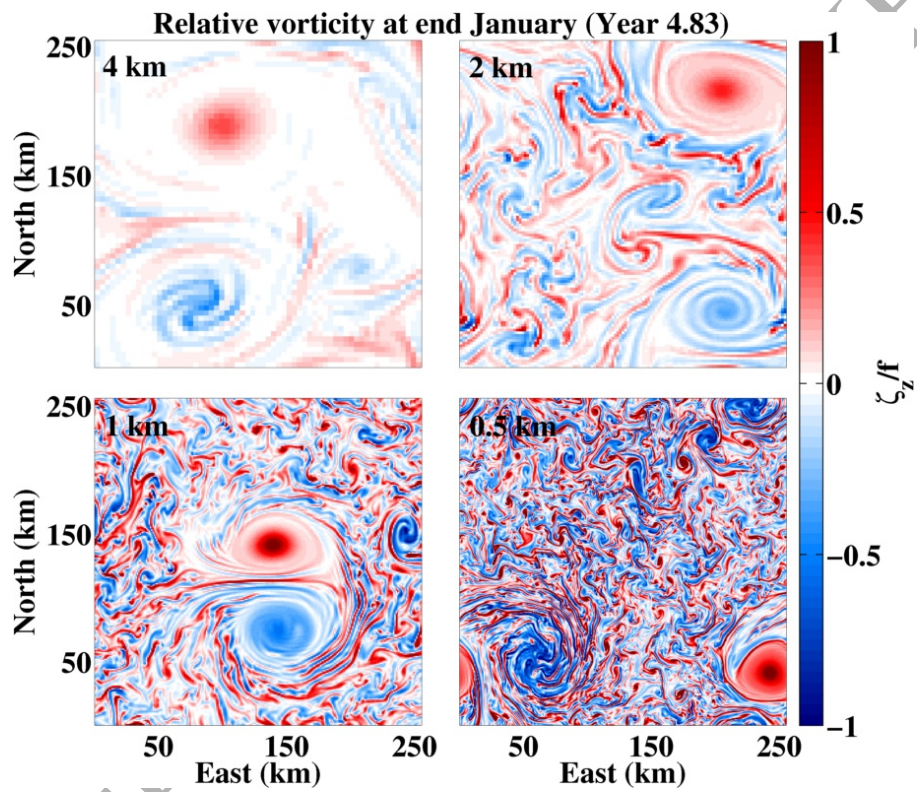


Figure 10: A snapshot of the vertical component of relative vorticity at the surface. The panels are at the indicated grid resolutions, though the labels are somewhat obscured in the lower panels. As for Figure 5, the snapshots are derived from the model state in late January (year 4.83) when the mean mixed layer is approximately 90 m deep.

314 *3.4. Momentum balance*

315 The various balances of momentum give an understanding of how the dy-
316 namics differ across resolutions and through the seasonal cycle. Following Capet
317 et al. (2008b), a metric for geostrophic balance is:

$$\epsilon_{geo}(\mathbf{x}, t) = 1 - \frac{|f\zeta_z - \frac{1}{\rho}\nabla_h^2 p|}{f|\zeta_z| + |\frac{1}{\rho}\nabla_h^2 p| + \mu_{geo}}, \quad (3.1)$$

318 where $\zeta_z = v_x - u_y$ is the vertical component of relative vorticity, p is pressure
319 and $\mu_{geo} = f\zeta_{z,RMS} + \rho^{-1}\nabla_h^2 p_{RMS}$ is a small constant included to avoid spurious
320 large values in areas of weak force balance. Note that the scale has been reversed
321 from Capet et al. (2008b) such that $\epsilon_{geo} = 1$ means full geostrophic balance.

322 Capet et al. (2008b) also investigate a generalised cyclostrophic or gradient-
323 wind balance that includes the full non-linear advective terms:

$$\epsilon_{adv}(\mathbf{x}, t) = 1 - \frac{|f\zeta_z + \nabla_h \cdot (\mathbf{u}\nabla\mathbf{u}_h) - \frac{1}{\rho}\nabla_h^2 p|}{f|\zeta_z| + |\nabla_h \cdot (\mathbf{u}\nabla\mathbf{u}_h)| + |\frac{1}{\rho}\nabla_h^2 p| + \mu_{adv}}, \quad (3.2)$$

324 where $\mathbf{u} = (u, v, w)$ is the velocity vector and μ_{adv} is adapted from μ_{geo} to
325 include the contribution of the advective terms. A similar notation is adopted
326 for this term in the balances below. The advection terms include the centripetal
327 acceleration and so this non-linear balance may better describe the force balance
328 in vortices and at curved fronts.

329 The model solution also supports internal waves that lead to more rapid
330 accelerations than those associated with the geostrophic flow. Although the
331 inclusion of the time derivative means the momentum is no longer ‘balanced’,
332 the inclusion of the time derivative provides useful insight, as discussed below.
333 This ‘balance’ is called a ‘time-advection’ balance by including the divergence
334 of the time derivative of the horizontal velocities:

$$\epsilon_{time-adv}(\mathbf{x}, t) = 1 - \frac{|f\zeta_z + \nabla_h \cdot \mathbf{u}_{h,t} + \nabla_h \cdot (\mathbf{u}\nabla\mathbf{u}_h) - \frac{1}{\rho}\nabla_h^2 p|}{f|\zeta_z| + |\nabla_h \cdot \mathbf{u}_{h,t}| + |\nabla_h \cdot (\mathbf{u}\nabla\mathbf{u}_h)| + |\frac{1}{\rho}\nabla_h^2 p| + \mu_{time-adv}}, \quad (3.3)$$

335 where the subscript t denotes differentiation in time.

336 In a simulation of filamentogenesis in the Gulf Stream Gula et al. (2014) find
337 that the vertical viscous fluxes are of the same order as the vertical shear and
338 horizontal buoyancy gradient in thermal wind balance. They term this ‘turbu-
339 lent thermal wind balance’. This is quantified here as a ‘turbulent geostrophic
340 balance’ by modifying (3.1) as:

$$\epsilon_{tg}(\mathbf{x}, t) = 1 - \frac{|f\zeta_z + \nabla_h \cdot (\tau_z) + \nabla \cdot ((K\mathbf{u}_z)_z) - \frac{1}{\rho}\nabla_h^2 p|}{f|\zeta_z| + |\nabla_h \cdot (\tau_z)| + |\nabla_h \cdot ((K\mathbf{u}_z)_z)| + |\frac{1}{\rho}\nabla_h^2 p| + \mu_{tg}}, \quad (3.4)$$

341 where K is the vertical viscous coefficient that is set by the *KPP* scheme in
342 the mixing layer but is a constant below and τ_z is the wind stress divergence

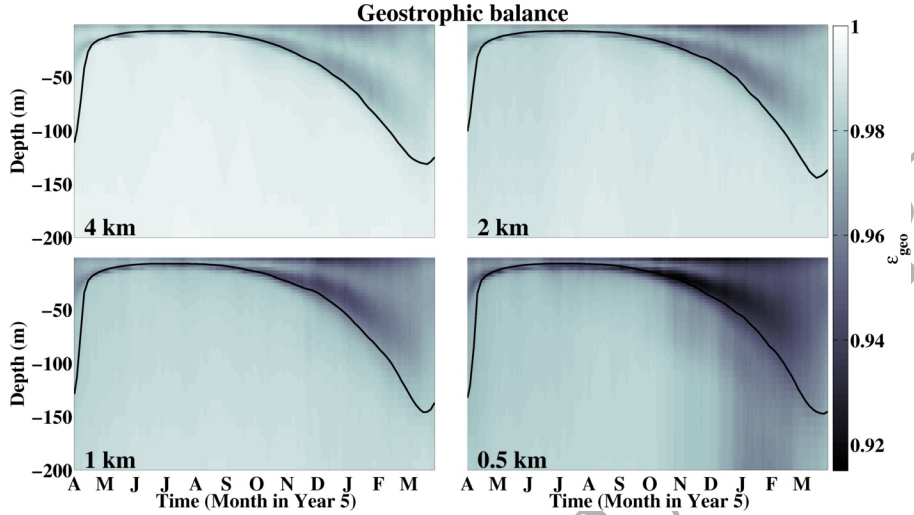


Figure 11: The degree of geostrophic balance $\overline{\epsilon_{geo}}$ calculated from snapshots of model output at 2-day intervals through the seasonal cycle. Darker colours indicate a departure from geostrophic balance. The black line is the mean mixed layer depth.

343 that accelerates the flow in the uppermost level. This is thus also a generalised
 344 version of the ‘turbulent Ekman balance’ of Taylor and Ferrari (2010).

345 Finally, to ascertain whether a full description of balance is being approached
 346 we can combine all of the terms from the turbulent and time-advection balances
 347 as:

$$\epsilon_{tta}(\mathbf{x}, t) = 1 - \frac{|f\zeta_z + \nabla_h \cdot (\tau_z) + \nabla_h \cdot ((K\mathbf{u}_z)_z) + \nabla_h \cdot \mathbf{u}_t + \nabla_h \cdot (\mathbf{u}\nabla_h\mathbf{u}) - \frac{1}{\rho}\nabla_h^2 p|}{f|\zeta_z| + |\nabla_h \cdot \mathbf{u}_t| + |\nabla_h \cdot ((K\mathbf{u}_z)_z)| + |\nabla_h \cdot (\mathbf{u}\nabla_h\mathbf{u})| + |\frac{1}{\rho}\nabla_h^2 p| + \mu_{tta}} \quad (3.5)$$

348 The annual cycle in $\overline{\epsilon_{geo}}$ is shown in Fig. 11. This shows that the degree of
 349 balance falls as the resolution is made finer, both in the mixed layer and in the
 350 interior. Vertically, the degree of balance is lower in the mixed layer than in
 351 the interior, though minima are often found at the base of the deepening mixed
 352 layer.

353 While geostrophic balance is the primary balance, there is a change in the
 354 residual mean balance across this range of resolutions. Figure 12 shows the vertical
 355 profiles of horizontal mean of the various balances in late January, when the
 356 mean mixed layer depth is approximately 90 m. This is during the time interval
 357 when $\overline{\epsilon_{geo}}$ is relatively low in the thermocline of the finest resolution case
 358 (Fig. 11, bottom-right panel). Comparing firstly the geostrophic balance, Fig.
 359 12 (top-left panel) shows again that the magnitude of $\overline{\epsilon_{geo}}$ falls as the resolution
 360 is made finer. Moving to the turbulent geostrophic balance (Fig. 12, top-right
 361 panel) improves the degree of balance over geostrophy alone. However, this

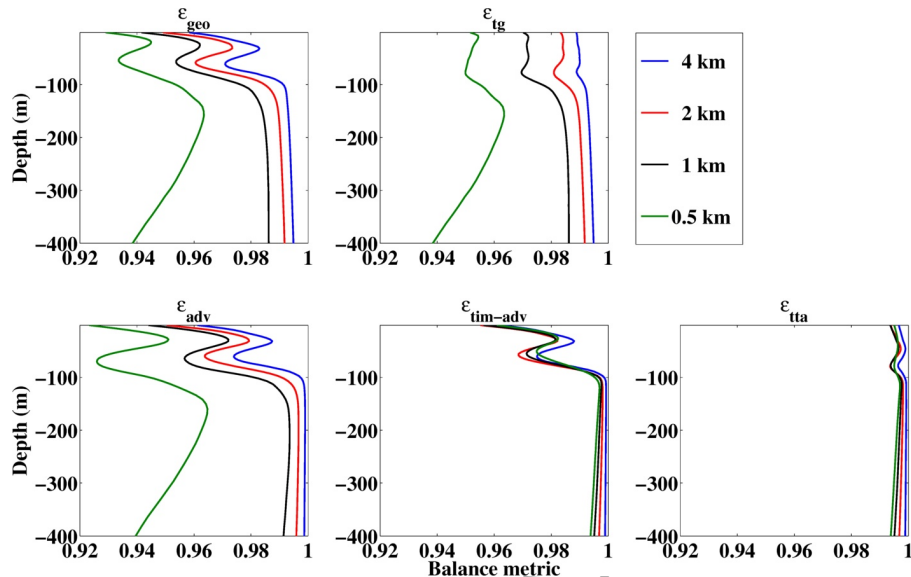


Figure 12: Vertical profiles of the balance parameters (x-axis in all panels) in late January (year 4.83) during the period of mixed layer deepening. The mean mixed layer is approximately 90 m at all resolutions. The calculation is based on a snapshot of model output. (Top left) Geostrophic balance as measured by $\overline{\epsilon_{geo}}$. (Top centre) Turbulent geostrophic balance as measured by $\overline{\epsilon_{tg}}$. (Bottom left) Advective balance as measured by $\overline{\epsilon_{adv}}$. (Bottom centre) Time-advective balance as measured by $\overline{\epsilon_{time-adv}}$. (Bottom right) Turbulent-linear-cyclostrophic balance as measured by $\overline{\epsilon_{tta}}$.

362 improvement in balance is only in the mixed layer, as the vertical diffusion of
 363 momentum in the interior is much weaker. Now comparing geostrophy and
 364 the advective balance $\overline{\epsilon_{adv}}$, Fig. 12 (left-hand panels) shows that incorporating
 365 advective terms improves the degree of balance by a small amount at coarser
 366 resolution. However, for the two finer resolutions the advective balance is actu-
 367 ally slightly less than the geostrophic balance near the base of the mean mixed
 368 layer at 90 m and the degree of balance does not materially improve with the ad-
 369 vective balance in the thermocline. In order to better describe the momentum
 370 ‘balance’ at the finest resolution, the time derivative terms must be included
 371 (centre panel, bottom row). In the coarser resolution runs, the addition of the
 372 time derivative term makes little difference and $\overline{\epsilon_{adv}} \approx \overline{\epsilon_{time-adv}}$. Therefore,
 373 the time derivative terms become an important part of the residual momentum
 374 balance in late winter at finer resolution in the mixed layer and thermocline.
 375 The combined balance terms in $\overline{\epsilon_{tta}}$ are shown in Fig. 12 (right panel, bottom
 376 row), with the residual accounted for by the horizontal diffusion of momentum
 377 in the mixed layer and a small factor due to the time-stepping scheme.

378 A physical sense for the change in the residual balance across resolutions can
 379 be gained by considering the geostrophic balance $\overline{\epsilon_{geo}}$ at the base of the mixed

380 layer in Figure 13. This is taken from the same time as the sea surface buoyancy
 381 gradients plot in Fig. 5 and the mean balances in Fig. 12. The advective and
 382 time derivative terms account for the departure from balance near (60 km,
 383 60 km) in Fig. 13 (bottom-right panel) and are thus associated with the long
 384 filamentary streaks that are wrapped into the large anti-cyclone there and visible
 385 as buoyancy gradients in Fig. 5. As such the filaments are indicative of an
 386 unbalanced process that is developing rapidly in time. The dynamical process
 387 that generates these filaments is considered in more detail in a forthcoming paper
 388 (Brannigan, in prep.). Such filamentation and the accompanying departure
 389 from geostrophic balance becomes weaker as the resolution becomes coarser
 390 (Fig. 13). Lower values of ϵ_{geo} are increasingly found in the large vortices at all
 391 resolutions as the resolution is made finer. It is here that the degree of balance is
 392 most improved by moving to advective balance ϵ_{geo} that includes the centripetal
 393 acceleration and so the mixed layer portion of the mesoscale vortices becomes
 394 more non-linear as the resolution is made finer. The improvement in balance in
 395 the mixed layer by the use of turbulent geostrophic balance, measured by ϵ_{tg} ,
 396 is relatively uniform through the domain (not shown).

397 4. Frontal processes

398 The results in Section 3 show that there are distinct differences across the
 399 resolutions in terms of the buoyancy, velocity and balances and growing sea-
 400 sonal differences between the runs. These differences are due to submesoscale
 401 processes, that are diagnosed individually here.

402 4.1. Frontogenesis

403 Although frontogenesis is formally defined to be the development of a dis-
 404 continuity in buoyancy at a front, it is taken here to mean the action by the flow
 405 field to increase or decrease the variance of horizontal buoyancy gradients. The
 406 impact of frontogenesis on horizontal gradients is diagnosed using the frontoge-
 407 nesis function (Hoskins and Bretherton, 1972) modified to include the vertical
 408 advective transport:

$$F_s = \mathbf{Q}_s \cdot \nabla_h b, \quad (4.1)$$

where:

$$\mathbf{Q}_s = -(u_x b_x + v_x b_y + w_x b_z, u_y b_x + v_y b_y + w_y b_z). \quad (4.2)$$

409 In agreement with Capet et al. (2008b), the mean magnitude of frontogenesis
 410 generally grows as the resolution becomes finer with level-mean values increasing
 411 by approximately a factor of two for each doubling in resolution (Figure 14, all
 412 panels). Of more novelty is the seasonal cycle in the magnitude of frontogenesis
 413 as the mixed layer depth varies by an order of magnitude from summer to winter.
 414 Figure 14 shows that $\overline{F_s}$ is low in the initial period of mixed layer restratification
 415 (April to June, all panels). It then grows in magnitude through the remainder
 416 of the summer and into autumn and early winter (August to December) before

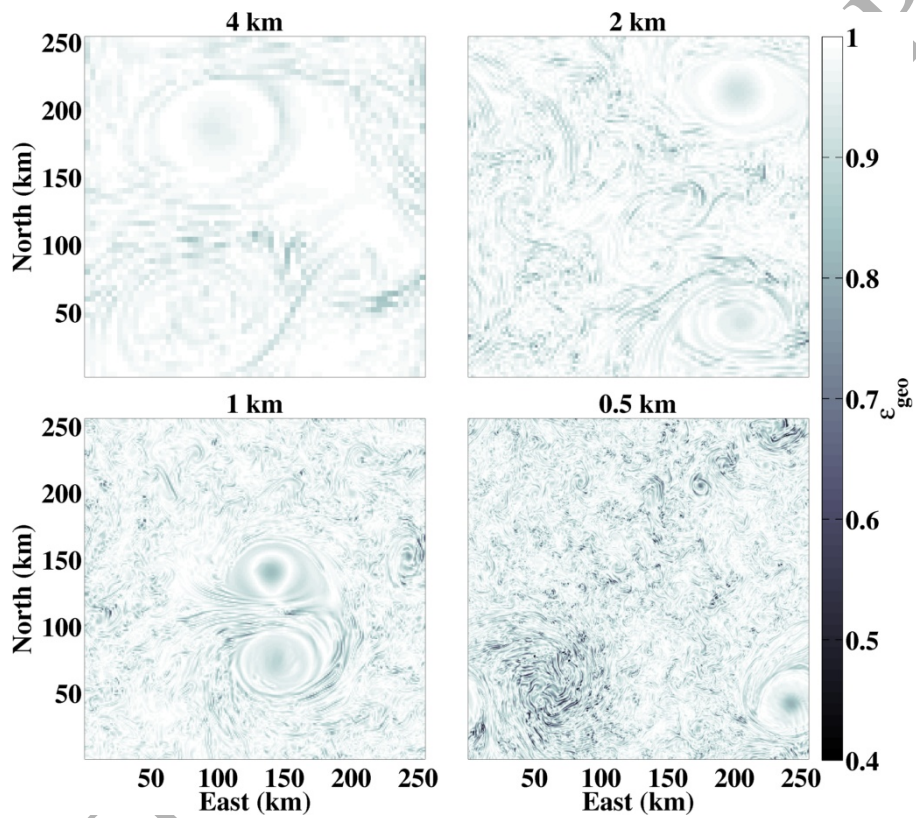


Figure 13: Plan views of the geostrophic balance parameter ϵ_{geo} near the base of the mean mixed layer at 74 m depth in late January (at year 4.83). Darker colours show departures from geostrophic balance. This is taken from the same time as the plot of sea surface buoyancy gradients in Figure 5 and the surface relative vorticity in Figure 10.

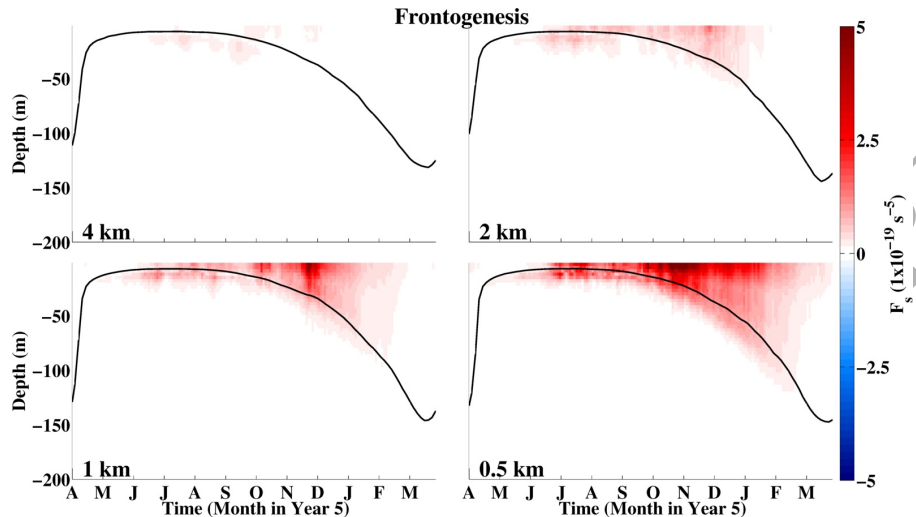


Figure 14: The level-mean value of the frontogenesis function, defined in equation (4.1), by model level over the fifth year of the simulations. The calculation is based on snapshots of model output at 2-day intervals. The black line shows the mean mixed layer depth at that time.

417 weakening in the late winter when the mixed layer deepens from 80 m to 150
 418 m. The weakening of $\overline{F_s}$ in winter (all panels) could reflect the ability of mixed
 419 layer instabilities to overturn strong buoyancy gradients when the mixed layer
 420 is of sufficient depth. The period in the annual cycle when $\overline{Q_s}$ begins to weaken
 421 coincides with the interval when the slope of the surface velocity spectra reaches
 422 its shallower values in Fig. 8 (bottom panel).

423 4.2. Ekman buoyancy fluxes

424 The creation or destruction of potential vorticity, taken to be the Ertel po-
 425 tential vorticity $q = (f + \nabla \times \mathbf{u}) \cdot \nabla b$, due to frictional forcing at the boundary
 426 has been established observationally and numerically as an important process
 427 at ocean fronts (Thomas, 2005; Capet et al., 2008b; Taylor and Ferrari, 2010;
 428 Mahadevan et al., 2010; D’Asaro et al., 2011). This process is referred to as the
 429 Ekman buoyancy flux (EBF) and can be diagnosed as:

$$EBF = \left(\frac{\tau}{\rho_o f} \times \mathbf{k} \right) \cdot \nabla_h b, \quad (4.3)$$

430 where τ is the wind stress, ρ_o is a reference density and \mathbf{k} is the unit vertical
 431 vector. The term $\nabla_h b$ is formally the mean buoyancy gradient over the Ekman
 432 layer, though we take it to be the surface buoyancy gradient. While the mean
 433 value of the EBF is notionally zero when averaged over a periodic domain, there
 434 is still a net effect on stratification as the down-front winds induce a vertical
 435 diffusive mixing through the whole mixed layer, while the up-front winds induce

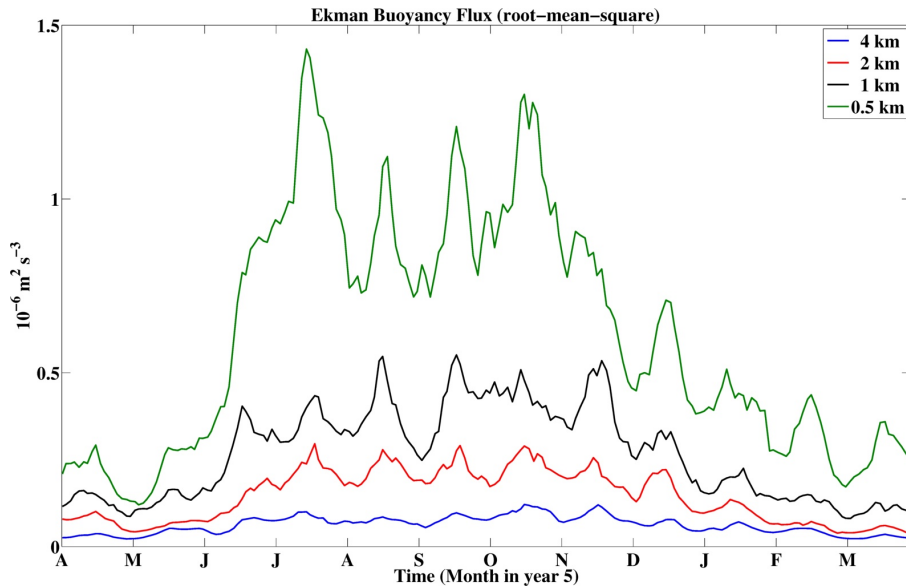


Figure 15: The root-mean-square magnitude of the Ekman buoyancy flux, defined in equation 4.3, over the fifth year of the simulations.

436 an advective restratification in the Ekman layer (Thomas and Ferrari, 2008). In
 437 locations of up-front winds, the Ekman layer is generally shallower than 30 m.

438 Fig. 15 shows that the root-mean-square Ekman buoyancy flux has a similar
 439 annual cycle to $\overline{F_s}$ in that its peak values occur in summer conditions when $|\nabla_h b|$
 440 is largest and it is stronger at finer resolution. The magnitude of the buoyancy
 441 fluxes is order $10^{-6} \text{ m}^2 \text{ s}^{-3}$ at fine resolution. This is some 20 times larger than
 442 the buoyancy flux due to the peak surface heating/cooling and emphasises the
 443 local importance of the EBF in setting stratification (Thomas and Ferrari, 2008;
 444 Thomas et al., 2013) even in these simulations where the mean wind stress is
 445 moderate compared to values achieved in the open ocean. Although the winds
 446 are relatively weak here, the magnitude of the horizontal buoyancy gradients
 447 that arise are much stronger. The oscillations in the EBF in Fig. 15 are the
 448 main consequence of the monthly cycle in the wind-forcing noted in Section 2.
 449 The effect of the EBF is investigated further in Section 4.3.

450 4.3. Instabilities of negative potential vorticity

451 The ocean is subject to a range of instabilities when $f q < 0$, which in
 452 these simulations is equivalent to negative potential vorticity. Where negative
 453 potential vorticity occurs, the dominant expected response to perturbations
 454 can be inferred from the balanced Richardson number Ri_b (defined in equation
 455 (4.4)). The infinite range of possible Ri_b can be contracted to an angle ϕ
 456 following the approach of Thomas et al. (2013) where a schematic can be found:

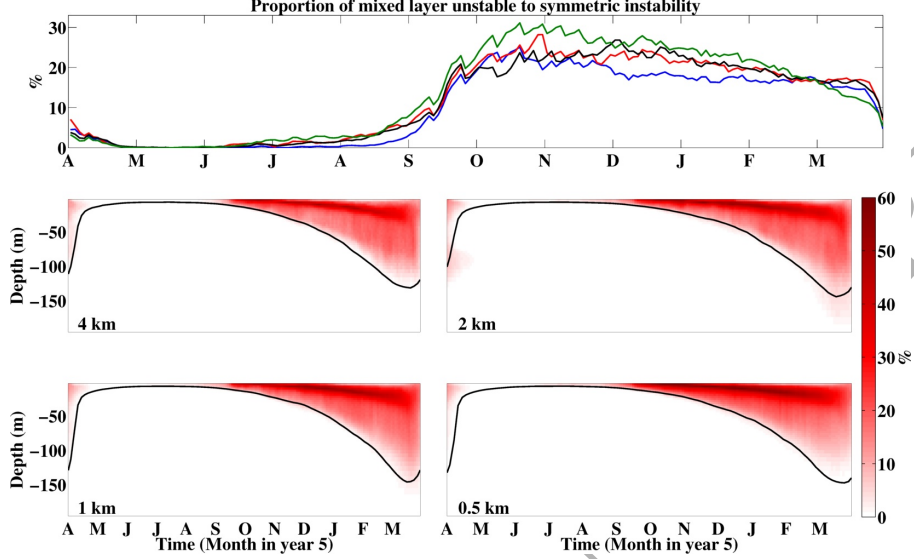


Figure 16: The proportion of the domain with negative potential vorticity where a pure or hybrid symmetric mode is predicted. (Top panel) The mean proportion of the mixed layer volume where symmetric instability is predicted. (Lower panels) The proportion of the levels where symmetric instability is predicted. Calculated based on snapshot model outputs taken at 2-day intervals during the fifth year of the simulation. The black line in the lower panels is the mean mixed layer depth.

$$\phi_{\text{Ri}_b} = \tan^{-1}(-\text{Ri}_b^{-1}) = \tan^{-1} \frac{-|\nabla_h b|^2}{f^2 N^2}, \quad (4.4)$$

and

$$\phi_{\text{Ri}_b} < \phi_c = \tan^{-1}(-\zeta_g/f), \quad (4.5)$$

where $\zeta_g = f + \nabla \times \mathbf{u}_g$ and \mathbf{u}_g is the geostrophic velocity. When $-180^\circ < \phi_{\text{Ri}_b} < -135^\circ$, the potential vorticity is negative due to unstable stratification and convective instability is expected to dominate. When $-135^\circ < \phi_{\text{Ri}_b} < -90^\circ$, the potential vorticity is negative due to both unstable stratification and horizontal buoyancy gradients and so a hybrid convective/symmetric mode is predicted. For stable stratification and cyclonic vorticity $-90^\circ < \phi_{\text{Ri}_b} < \phi_c$, with $\phi_c < -45^\circ$ implies that a symmetric instability should arise. For anti-cyclonic vorticity a symmetric mode is expected to dominate where $-90^\circ < \phi_{\text{Ri}_b} < -45^\circ$ and a hybrid symmetric-centrifugal instability is anticipated where $-45^\circ < \phi_{\text{Ri}_b} < \phi_c$.

It is cautioned that this analysis does not take into account the vertical velocity shear that arises due to surface waves. Haney et al. (Subm. to JPO) show that where the wind and waves are in the same direction, this leads to an increase in Ri_b . The balanced Richardson number here also assumes that there is no curvature to the flow.

471 Figure 16 (upper panel) shows that up to 30% of the mixed layer volume
 472 is unstable to pure or hybrid symmetric instabilities in winter conditions. The
 473 proportion of the mixed layer volume where such a condition holds grows some-
 474 what as the resolution is made finer, though the values are comparable across
 475 all resolutions. In the shallow mixed layers early in the restratification period
 476 (April - August in Fig. 16, upper panel) very little negative potential vorticity
 477 is found at any resolution due to the stratifying effect of the surface heating.
 478 The proportion of the domain where negative potential vorticity is found then
 479 grows in late summer (September - October in Fig. 16, upper panel). It reaches
 480 its peak value quite early in the winter by November at all resolutions before
 481 gradually decreasing in late winter despite the continual cooling.

482 The vertical distribution of negative potential vorticity is shown in Fig. 16
 483 (lower panels) and is similar at all resolutions. The lower panels shows that the
 484 occurrence of negative potential vorticity is essentially limited to the mean mixed
 485 layer. The distribution of negative potential vorticity is not concentrated in the
 486 Ekman layer reflecting the tendency for down-front winds to induce vertical
 487 mixing and so extract potential vorticity throughout the mixed layer (Thomas
 488 and Ferrari, 2008) when using *KPP*, though simulations with resolved boundary
 489 layer turbulence show that the extraction of potential vorticity may be concen-
 490 trated in a shallower layer (Taylor and Ferrari, 2010; Hamlington et al., 2014).
 491 The peak proportion of the mixed layer volume that is most unstable to cen-
 492 trifugal instability grows from 1% of the mixed layer volume at the coarsest
 493 resolution to 4% at the finest resolution (not shown). In addition, the upper 10
 494 m of the model domain develops a slight negative stratification in the cooling
 495 period at all resolutions. This negative stratification in the upper levels is a
 496 typical feature of numerical simulations.

497 As for Capet et al. (2008b), regions of negative potential vorticity are pro-
 498 duced by the down-front wind mechanism driven by the zonal wind stress. Fig-
 499 ure 17 shows the mean potential vorticity for a given zonal or meridional buoy-
 500 ancancy gradient based on a snapshot of model output at the end of December
 501 in year 5 at 9 m depth. The top row in Fig. 17 shows no systematic relation-
 502 ship between the zonal buoyancy gradient and potential vorticity. However, the
 503 bottom row shows that there is a near-linear relationship between the merid-
 504 ional buoyancy gradient and potential vorticity at all resolutions. When $b_y < 0$,
 505 colder water lies to the north of warmer water. Given the mean zonal wind,
 506 $b_y < 0$ corresponds to a down-front wind (Thomas, 2005) and mean potential
 507 vorticity is indeed negative in this case. On the other hand, where $b_y > 0$ the
 508 wind is up-front and mean potential vorticity is positive in this case. This effect
 509 becomes stronger as the resolution is made finer (Fig. 17, lower panels). The
 510 seasonal cycle in the proportion of the mixed layer unstable to symmetric in-
 511 stability (Fig. 16, upper panel) partly reflects the seasonal cycle in horizontal
 512 buoyancy gradients. When horizontal buoyancy gradients are stronger in the
 513 late summer and autumn (Fig. 6) the conditions for symmetric instability are
 514 most commonly found. As the horizontal buoyancy gradients weaken in late
 515 winter, less symmetric instability is expected.

516 A similar analysis can be carried out in Fig. 17 where the potential vorticity

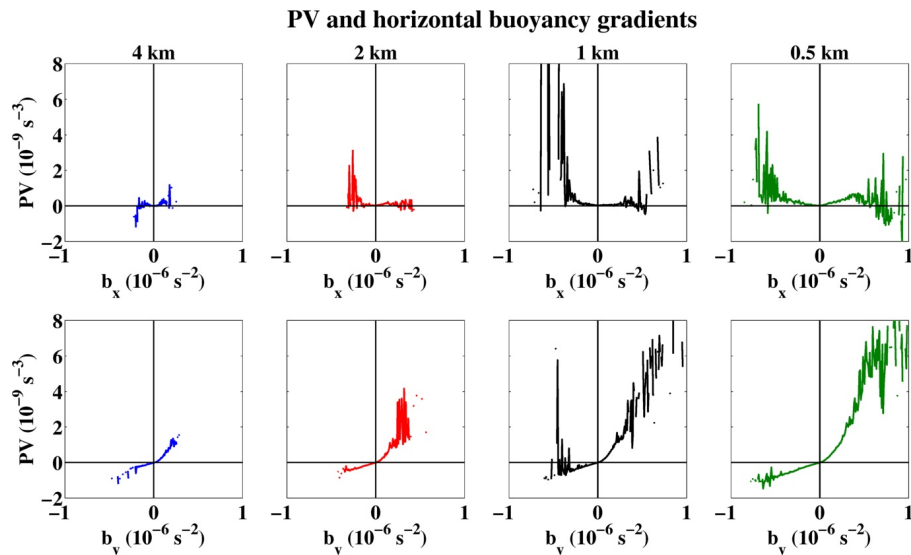


Figure 17: The mean potential vorticity for a given horizontal buoyancy gradient at 9 m depth at in late December. (Top row) The mean potential vorticity for a given zonal buoyancy gradient. (Bottom row) The mean potential vorticity for a given meridional buoyancy gradient. These results are consistent with Fig. 11 of Capet et al. (2008b).

517 is compared to the Okubo-Weiss parameter $S^2 - \zeta_z^2$, where $S^2 = (v_x + u_y)^2 +$
 518 $(u_x - v_y)^2$ is the strain. No systematic relationship between the Okubo-Weiss
 519 parameter and potential vorticity is found (not shown). This can be understood
 520 by considering the horizontal distribution of negative potential vorticity at the
 521 end of December in Figure 18. This figure illustrates that negative values of
 522 potential vorticity are found both inside as well as outside the vortices, for
 523 example at (100 km, 80 km) at 4 km resolution in the upper-left panel or at
 524 (110 km, 160 km) in the lower-right panel. Negative potential vorticity in the
 525 large vortices correspond to regions of negative meridional buoyancy gradients
 526 within the vortices. A forthcoming paper (Brannigan, in prep.) shows that
 527 the negative potential vorticity within the vortices leads to strong symmetric
 528 instabilities there.

529 4.4. Vertical advective fluxes

530 The magnitude of the vertical buoyancy fluxes is $\overline{w'b'}$, where w is the vertical
 531 velocity, b is the buoyancy and primes indicate a departure from the level mean.
 532 The second panel in Figure 19 shows that vertical buoyancy fluxes averaged over
 533 the mixed layer become stronger as the resolution becomes finer and has its peak
 534 in December and January. As such the seasonal cycle in vertical advective fluxes
 535 differs from the diagnosed seasonal cycle in frontogenesis and Ekman buoyancy
 536 fluxes. The lower panels in Fig. 19 show the vertical profiles of $\overline{w'b'}$ and show

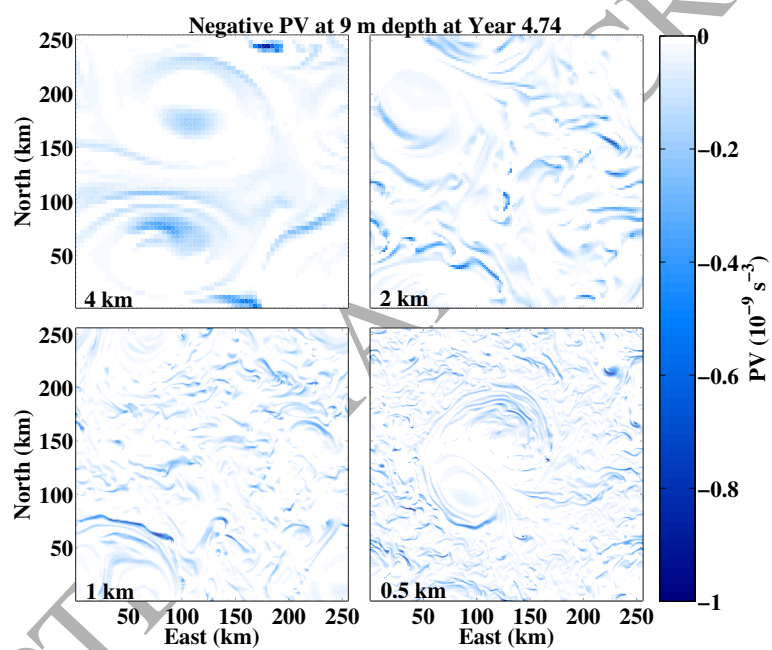


Figure 18: Plan-view plots of negative potential vorticity at 9 m depth in late December at the indicated resolution. The colorscale saturates at $q = 0$ so regions of positive potential vorticity are shown in white.

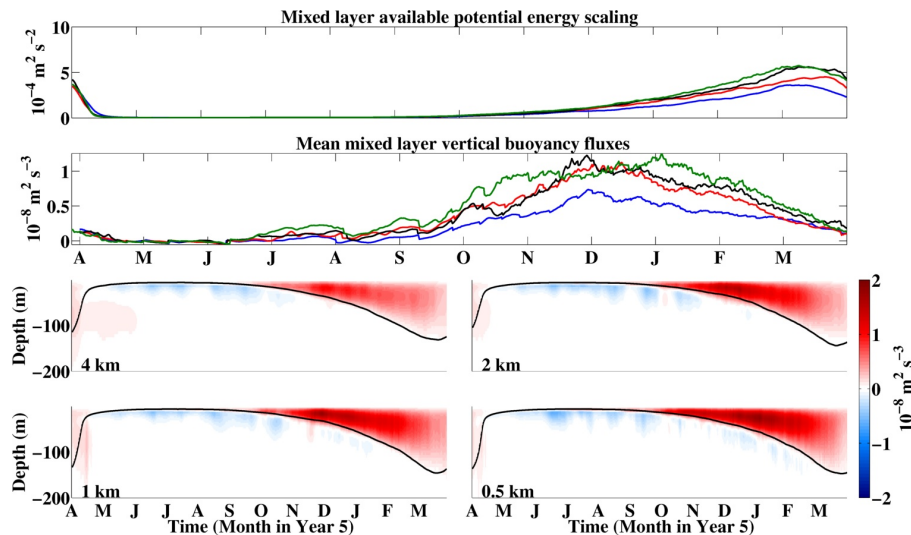


Figure 19: The available potential energy and the mean vertical advective buoyancy flux $\overline{w'b'}$ over the fifth year of the simulations. (Upper panel) The mean available potential energy in the mixed layer $\overline{APE} = \overline{H^2|\nabla_h b|}$ at 12 hour intervals, where H is the mixed layer depth. (Second panel) The flux integrated over the mean mixed layer with a colour scheme as for Fig. 4. (Lower panels) The vertical profile of the mean vertical advective fluxes at the resolution indicated. The vertical flux is averaged by model level and in six-hour intervals online. The black line in the lower panels shows the mean mixed layer depth at that time.

537 that the most intense vertical fluxes occur in December, when the mean mixed
 538 layer is just 55 m deep. This is the same time period that the slope of the
 539 surface velocity power spectral density arrives at its winter value close to -2
 540 (Fig. 8). There are negative vertical buoyancy fluxes below the mean mixed layer
 541 throughout the year. An initial hypothesis is that the negative vertical buoyancy
 542 fluxes arise due to the spatial structure of the wind forcing employed. However,
 543 the negative vertical buoyancy fluxes are present if the model is forced only with
 544 the uniform zonal wind after it has been spun up and so the spatial structure of
 545 the wind forcing can be ruled out as the cause of the negative buoyancy fluxes.
 546 These negative buoyancy fluxes appear to be associated with regions of negative
 547 potential vorticity and are investigated further in a forthcoming paper.

548 The analysis in Section 4.3 shows that up to 30% of the mixed layer experi-
 549 ences negative potential vorticity during the winter. Thus the majority of the
 550 mixed layer has positive potential vorticity and so mixed layer baroclinic insta-
 551 bilities are expected to be the dominant component of the vertical advective
 552 fluxes (Stone, 1966; Molemaker et al., 2005; Boccaletti et al., 2007; Fox-Kemper
 553 et al., 2008; Skillingstad and Samelson, 2012; Bachman and Fox-Kemper, 2013;
 554 Brüggemann and Eden, 2014). The importance of these instabilities can be
 555 estimated through the seasonal cycle by scaling the potential energy available

556 for release. We employ the central concept of the Fox-Kemper et al. (2008)
 557 parameterisation by estimating the magnitude of the available potential energy:

$$APE = H^2 |\nabla_h b|, \quad (4.6)$$

558 where H is the mixed layer depth. This is shown in Figure 19 (top panel)
 559 where the seasonal cycle in APE is somewhat different that that of the vertical
 560 buoyancy fluxes, as the vertical buoyancy fluxes peak earlier in winter than the
 561 APE. The peak in vertical buoyancy fluxes before the peak in APE could reflect
 562 other factors such as the effect of strain on the growth of baroclinic instability
 563 (Bishop, 1993; Spall, 1997; McWilliams and Molemaker, 2011), as some of the
 564 highest APE is found in the confluence region between mesoscale eddies where
 565 the fronts do not have meanders indicative of baroclinic waves. An example of
 566 this is the straight front that runs along $y = 75$ km in the lower-left panel of
 567 Fig. 5. Flow curvature could also affect the growth of baroclinic eddies, as the
 568 APE metric is high in and around cyclonic eddies, where again there is limited
 569 evidence that baroclinic instability occurring, for example around the cyclonic
 570 eddy centred at (250 km, 40 km) in the lower-right panel of Fig. 5.

571 5. Discussion

572 The results of a series of multi-year simulations in a domain analogous to
 573 the mid-latitude open ocean show a significant seasonal cycle in submesoscale
 574 flows and this seasonal cycle becomes more pronounced as the resolution is made
 575 finer. The slopes of horizontal spectra of SST and surface velocity are steep in
 576 summer when the mixed layer is less than 20 m deep and then rapidly become
 577 shallower as the mixed layer deepens. The shallowing of the velocity spectra
 578 stops when the mixed layer is just 40 m deep, suggesting that the dynamical
 579 regime reflected by this shallower slope does not require particularly deep mixed
 580 layers.

581 The simulations also vary across the range of resolutions. As the resolution is
 582 increased, sharper fronts emerge and the residual momentum balance of the flow
 583 includes a larger contribution from advective and rapidly-developing motions.
 584 Processes at ocean fronts including frontogenesis and Ekman buoyancy fluxes are
 585 found to strengthen as the resolution is made finer. The prevalence of negative
 586 potential vorticity does not increase monotonically with resolution, but instead
 587 depends on the flow configuration at a given time. The stronger frontogenetical
 588 processes lead to more available potential energy as the resolution is made finer
 589 and stronger advective vertical buoyancy fluxes in winter.

590 Both available potential energy and vertical buoyancy fluxes in the mixed
 591 layer are stronger in winter and so we conclude that overturning instabilities such
 592 as baroclinic instability or symmetric instability are the primary driver of these
 593 vertical buoyancy fluxes, rather than the fluxes associated with frontogenesis or
 594 Ekman pumping. Mixed layer vertical buoyancy fluxes peak in mid-winter, while
 595 the available potential energy peaks in late winter. This may reflect other factors
 596 such as strain, vorticity or curvature (Bishop, 1993; Spall, 1997; McWilliams and

597 Molemaker, 2011; Thomas, 2012) that affect stability in addition to horizontal
598 buoyancy gradients. The different seasonal cycles between the vertical buoyancy
599 fluxes and frontogenesis suggests that the balance between frontogenesis and
600 mixed layer baroclinic instabilities (e.g. McWilliams and Molemaker, 2011) may
601 be quite sensitive to the vertical scale height with frontogenesis stronger when
602 the mixed layer is shallow and baroclinic instabilities stronger as the mixed layer
603 deepens for a given horizontal buoyancy gradient and strain.

604 Recent numerical and observational studies also find that the spectral slope
605 of velocity in the mixed layer shallows in winter (Mensa et al., 2013; Sasaki
606 et al., 2014; Callies et al., 2015). These studies interpret this result as the con-
607 sequence of frontogenesis and mixed layer baroclinic instabilities considered by
608 Boccaletti et al. (2007). However, the results in Section 4.3 show that 30% of
609 the mixed layer volume has negative potential vorticity and is therefore most
610 unstable to symmetric instability. As such, it is possible that the submesoscale
611 length range is energised by symmetric instability in addition to baroclinic in-
612 stability and frontogenesis. Extensive symmetric instability could have impli-
613 cations for describing mixed layer flows in terms of quasi-geostrophic or surface
614 quasi-geostrophic models, as the flow associated with symmetric instability is
615 unbalanced (Stone, 1966) and so cannot be captured by theories based on bal-
616 anced dynamics in their standard forms.

617 The question of convergence of the simulations over this range of resolutions
618 remains open. The similar seasonal cycle in spectral slopes in the three finer
619 resolution cases can be used to argue for convergence, as per Capet et al. (2008a).
620 However, the diagnosed submesoscale processes continue to become stronger as
621 the resolution is made finer and the mean stratification profile varies throughout
622 the range of resolutions employed in Fig. 4. Furthermore, Bachman and Taylor
623 (2014) show that the degree to which symmetric instability is resolved changes
624 markedly over this range of resolutions and so this also affects the subsequent
625 development of stratification as the resolution is refined. The inclusion of surface
626 waves and Langmuir turbulence also significantly affects the vertical fluxes and
627 stratification (Hamlington et al., 2014; Haney et al., Subm. to JPO).

628 The results show that some departures from geostrophic balance are found
629 in the domain. In particular, there is a departure from geostrophy in the mixed
630 layer of the large vortices where non-linear effects due to the centripetal accelera-
631 tion should also be taken into account, in agreement with the results of Douglass
632 and Richman (2015). The model solutions also show that the momentum bal-
633 ance in the mixed layer includes a component due to the vertical diffusion of
634 momentum, though a more accurate description requires taking into account
635 the physics of the unresolved processes (Taylor and Ferrari, 2010; McWilliams
636 and Fox-Kemper, 2013; Hamlington et al., 2014).

637 There are of course a number of limitations to this study in addition to those
638 discussed above such as the artificial structure of the wind forcing. The grid
639 resolutions employed require the use of a vertical mixed layer parameterisation
640 and so important effects like the convective layer depth (Taylor and Ferrari,
641 2010; Thomas et al., 2013), interaction with small-scale turbulence (Skylingstad
642 and Samelson, 2012), or surface wave effects (McWilliams and Fox-Kemper,

2013; Hamlington et al., 2014; Haney et al., Subm. to JPO) could not be explored. The surface boundary conditions are imposed and so do not allow SST anomalies to generate differential air-sea fluxes. In addition, it is often the case that the internal wave field in such model studies is less energetic than in the real ocean (Shcherbina et al., 2013), due to the wind forcing being sub-inertial and the lack of tides and topography (Callies and Ferrari, 2013). The contribution of the time derivative terms to the residual balance shows, however, that internal waves are generated due to unbalanced motions (Shakespeare and Taylor, 2013).

To follow on from this work, the presence of submesoscale filaments inside mesoscale vortices will be examined in more detail (Brannigan, in prep.). The development of stratification in the model as the resolution varies will also be investigated to illustrate why a deeper mixed layer develops at finer resolution. These predictions will also be tested with the OSMOSIS mooring array from the North Atlantic.

Acknowledgements

This work forms part of the OSMOSIS project funded by the Natural Environment Research Council. We thank David Munday for assistance with running the experiment. The responses of Baylor Fox-Kemper and two anonymous reviewers have greatly improved the manuscript along with helpful comments from Andy Thompson, Ayah Lazar, Andy Hogg, Joern Callies and our colleagues in the OSMOSIS consortium. This work used the ARCHER UK National Supercomputing Service.

References

- Arbic, B. K., Scott, R. B., 2008. On quadratic bottom drag, geostrophic turbulence, and oceanic mesoscale eddies. *J.Phys.Oceanogr.* 38 (1), 84–103.
- Bachman, S., Fox-Kemper, B., Apr. 2013. Eddy parameterization challenge suite I: Eady spindown. *Ocean Modelling* 64, 12–28.
URL <http://linkinghub.elsevier.com/retrieve/pii/S1463500312001801>
- Bachman, S., Taylor, J., Oct. 2014. Modelling of partially-resolved oceanic symmetric instability. *Ocean Modelling* 82, 15–27.
URL <http://linkinghub.elsevier.com/retrieve/pii/S1463500314000961>
- Belcher, S. E., Grant, A. L., Hanley, K. E., Fox-Kemper, B., Van Roekel, L., Sullivan, P. P., Large, W. G., Brown, A., Hines, A., Calvert, D., 2012. A global perspective on langmuir turbulence in the ocean surface boundary layer. *Geophys.Res.Lett.* 39 (18).
- Berry, D. I., Kent, E. C., 2009. A new air-sea interaction gridded dataset from icoads with uncertainty estimates. *Bull.Am.Meteorol.Soc.* 90 (5), 645–656.

- 681 Bishop, C. H., 1993. On the behaviour of baroclinic waves undergoing horizontal
682 deformation. II: Error [U+2010]blind amplification and Rossby wave diagnos-
683 tics. *Q.J.R.Meteorol.Soc.* 119 (510), 241–267.
- 684 Boccaletti, G., Ferrari, R., Fox-Kemper, B., Sep. 2007. Mixed Layer Instabilities
685 and Restratification. *Journal of Physical Oceanography* 37 (9), 2228–2250.
686 URL <http://journals.ametsoc.org/doi/abs/10.1175/JP03101.1>
- 687 Brannigan, L., in prep. Intense upwelling in mesoscale eddies.
- 688 Brüggemann, N., Eden, C., 2014. Evaluating different parameterizations for
689 mixed layer eddy fluxes induced by baroclinic instability. *J.Phys.Oceanogr.*
690 44 (9), 2524–2546.
- 691 Callies, J., Ferrari, R., 2013. Interpreting energy and tracer spectra of upper-
692 ocean turbulence in the submesoscale range (1200 km). *J.Phys.Oceanogr.*
693 43 (11), 2456–2474.
- 694 Callies, J., R., F., Klymak, J. M., Mol, 2015. Seasonality in submesoscale tur-
695 bulence. *Nature Communications* In press.
- 696 Capet, X., McWilliams, J., Molemaker, M., Shchepetkin, A., 2008a. Mesoscale
697 to submesoscale transition in the California Current System. Part I: Flow
698 structure, eddy flux, and observational tests. *J.Phys.Oceanogr.* 38 (1), 29–43.
- 699 Capet, X., McWilliams, J., Molemaker, M., Shchepetkin, A., 2008b. Mesoscale
700 to submesoscale transition in the California Current System. Part II: Frontal
701 processes. *J.Phys.Oceanogr.* 38 (1), 44–64.
- 702 Capet, X., McWilliams, J., Molemaker, M., Shchepetkin, A., 2008c. Mesoscale
703 to submesoscale transition in the California current system. Part III: Energy
704 balance and flux. *J.Phys.Oceanogr.* 38 (10), 2256–2269.
- 705 Dale, A. C., Barth, J. A., Levine, M. D., Austin, J. A., Jan. 2008. Observa-
706 tions of mixed layer restratification by onshore surface transport following
707 wind reversal in a coastal upwelling region. *Journal of Geophysical Research*
708 113 (C1), C01010.
709 URL <http://doi.wiley.com/10.1029/2007JC004128>
- 710 Damerell, G. M., Heywood, K. J., Binetti, U., Kaiser, J., Thompson, A. F., in
711 prep. for *Geophys.Res.Lett.* Upper ocean variability at the Porcupine Abyssal
712 Plain time series site during 2012-2013.
- 713 D’Asaro, E., Lee, C., Rainville, L., Harcourt, R., Thomas, L., Apr. 2011.
714 Enhanced Turbulence and Energy Dissipation at Ocean Fronts. *Science*
715 332 (6027), 318–322.
- 716 Douglass, E. M., Richman, J. G., 2015. Analysis of ageostrophy in strong surface
717 eddies in the atlantic ocean. *J. Geophys. Res. Oceans* 120 (3), 1490–1507.
718 URL <http://dx.doi.org/10.1002/2014JC010350>

- 719 Fox-Kemper, B., Ferrari, R., Hallberg, R., Jun. 2008. Parameterization of Mixed
720 Layer Eddies. Part I: Theory and Diagnosis. *Journal of Physical Oceanogra-*
721 *phy* 38 (6), 1145–1165.
722 URL <http://journals.ametsoc.org/doi/abs/10.1175/2007JP03792.1>
- 723 Fox-Kemper, B., Menemenlis, D., 2013. Can large eddy simulation techniques
724 improve mesoscale rich ocean models? In: *Ocean Modeling in an Eddying*
725 *Regime*. American Geophysical Union, pp. 319–337.
726 URL <http://dx.doi.org/10.1029/177GM19>
- 727 Graham, J. P., Ringler, T., 2013. A framework for the evaluation of turbulence
728 closures used in mesoscale ocean large-eddy simulations. *Ocean Modelling* 65,
729 25–39.
- 730 Grant, A. L. M., Belcher, S. E., Aug. 2009. Characteristics of Langmuir Tur-
731 bulence in the Ocean Mixed Layer. *Journal of Physical Oceanography* 39 (8),
732 1871–1887.
733 URL <http://journals.ametsoc.org/doi/abs/10.1175/2009JP04119.1>
- 734 Griffies, S. M., Hallberg, R. W., 2000. Biharmonic friction with a Smagorinsky-
735 like viscosity for use in large-scale eddy-permitting ocean models. *Monthly*
736 *Weather Review* 128 (8), 2935–2946.
- 737 Gula, J., Molemaker, M. J., McWilliams, J. C., Oct. 2014. Submesoscale Cold
738 Filaments in the Gulf Stream. *Journal of Physical Oceanography* 44 (10),
739 2617–2643.
740 URL <http://journals.ametsoc.org/doi/abs/10.1175/JP0-D-14-0029.1>
- 741 Haine, T. W. N., Marshall, J., 1998. Gravitational, symmetric, and baroclinic
742 instability of the ocean mixed layer. *J.Phys.Oceanogr.* 28 (4), 634–658.
- 743 Hamlington, P. E., Van Roekel, L. P., Fox-Kemper, B., Julien, K., Chini,
744 G. P., Sep. 2014. Langmuir–Submesoscale Interactions: Descriptive Analysis
745 of Multiscale Frontal Spindown Simulations. *Journal of Physical Oceanogra-*
746 *phy* 44 (9), 2249–2272.
747 URL <http://journals.ametsoc.org/doi/abs/10.1175/JP0-D-13-0139.1>
- 748 Haney, S., Bachman, S., Cooper, B., Kupper, S., McCaffrey, K., Van Roekel, L.,
749 Stevenson, S., Fox-Kemper, B., Ferrari, R., 2012. Hurricane wake restratifi-
750 cation rates of one-, two- and three-dimensional processes. *J.Mar.Res.* 70 (6),
751 824–850.
- 752 Haney, S., Fox-Kemper, B., Julien, K., Webb, A., Subm. to JPO. Symmetric
753 and Geostrophic Instabilities in the Wave-Forced Ocean Mixed Layer.
- 754 Hill, C., Ferreira, D., Campin, J.-M., Marshall, J., Abernathey, R., Barrier,
755 N., 2012. Controlling spurious diapycnal mixing in eddy-resolving height-
756 coordinate ocean models - Insights from virtual deliberate tracer release ex-
757 periments. *Ocean Modelling* 45-46, 14–26.

- 758 Hosegood, P., Gregg, M. C., Alford, M. H., Nov. 2006. Sub-mesoscale lateral
759 density structure in the oceanic surface mixed layer. *Geophysical Research*
760 *Letters* 33 (22), L22604.
761 URL <http://doi.wiley.com/10.1029/2006GL026797>
- 762 Hoskins, B. J., Bretherton, 1972. Atmospheric Frontogenesis Models - Mathe-
763 matical Formulation and Solution. *Journal of the Atmospheric Sciences* 29 (1),
764 11–37.
- 765 Ilicak, M., Adcroft, A. J., Griffies, S. M., Hallberg, R. W., 2012. Spurious
766 dianeutral mixing and the role of momentum closure. *Ocean Modelling* 45-46,
767 37–58.
- 768 Koszalka, I., Bracco, A., McWilliams, J. C., Provenzale, A., Aug. 2009. Dy-
769 namics of wind-forced coherent anticyclones in the open ocean. *Journal of*
770 *Geophysical Research* 114 (C8), C08011.
771 URL <http://doi.wiley.com/10.1029/2009JC005388>
- 772 Lapeyre, G., Klein, P., Hua, B. L., 2006. Oceanic restratification forced by
773 surface frontogenesis. *Journal of Physical Oceanography* 36 (8), 1577–1590.
- 774 Large, W. G., McWilliams, J. C., Doney, S. C., 1994. Oceanic Vertical Mixing
775 - a Review and a Model with a Nonlocal Boundary-Layer Parameterization.
776 *Reviews of Geophysics* 32 (4), 363–403.
- 777 Leith, C. E., 1996. Stochastic models of chaotic systems. *Physica D* 98 (2-4),
778 481–491.
- 779 Lévy, M., Klein, P., a. M. Tréguier, Iovino, D., Madec, G., Masson, S.,
780 Takahashi, K., Jan. 2010. Modifications of gyre circulation by sub-mesoscale
781 physics. *Ocean Modelling* 34 (1-2), 1–15.
782 URL <http://linkinghub.elsevier.com/retrieve/pii/S1463500310000582>
- 783 Mahadevan, A., 2006. Modeling vertical motion at ocean fronts: Are nonhydro-
784 static effects relevant at submesoscales? *Ocean Modelling* 14 (3-4), 222–240.
- 785 Mahadevan, A., Tandon, A., Ferrari, R., Mar. 2010. Rapid changes in mixed
786 layer stratification driven by submesoscale instabilities and winds. *Journal of*
787 *Geophysical Research-Oceans* 115, C03017.
- 788 Marshall, J., Adcroft, A., Hill, C., Perelman, L., Heisey, C., 1997. A finite-
789 volume, incompressible Navier Stokes model for studies of the ocean on paral-
790 lel computers. *Journal of Geophysical Research-Oceans* 102 (C3), 5753–5766.
- 791 Marshall, J., Schott, F., 1999. Open ocean convection: Observations, theory,
792 and models. *Rev.Geophys.* 37 (1), 1–64.
- 793 McWilliams, J. C., Fox-Kemper, B., 2013. Oceanic wave-balanced surface fronts
794 and filaments. *J.Fluid Mech.* 730, 464–490.

- 795 McWilliams, J. C., Molemaker, M. J., Mar. 2011. Baroclinic Frontal Arrest: A
796 Sequel to Unstable Frontogenesis. *Journal of Physical Oceanography* 41 (3),
797 601–619.
798 URL <http://journals.ametsoc.org/doi/abs/10.1175/2010JP04493.1>
- 799 Mensa, J. A., Garraffo, Z., Griffa, A., Özgökmen, T. M., Haza, A., Veneziani,
800 M., Jul. 2013. Seasonality of the submesoscale dynamics in the Gulf Stream
801 region. *Ocean Dynamics* 63 (8), 923–941.
802 URL <http://link.springer.com/10.1007/s10236-013-0633-1>
- 803 Molemaker, M. J., McWilliams, J. C., Yavneh, I., Sep. 2005. Baroclinic instabil-
804 ity and loss of balance. *Journal of Physical Oceanography* 35 (9), 1505–1517.
- 805 Nastrom, G., Gage, K. S., 1985. A climatology of atmospheric wavenumber spec-
806 tra of wind and temperature observed by commercial aircraft. *J.Atmos.Sci.*
807 42 (9), 950–960.
- 808 Nurser, A. J. G., Zhang, J. W., 2000. Eddy-induced mixed layer shallowing and
809 mixed layer/thermocline exchange. *J. Geophys. Res.* 105 (C9), 21851–21868.
810 URL <http://dx.doi.org/10.1029/2000JC900018>
- 811 Painter, S. C., Pidcock, R. E., Allen, J. T., 2010. A mesoscale eddy driving spa-
812 tial and temporal heterogeneity in the productivity of the euphotic zone of the
813 northeast Atlantic. *Deep Sea Research Part II: Topical Studies in Oceanog-*
814 *raphy* 57 (15), 1281–1292.
- 815 Prather, M. J., 1986. Numerical advection by conservation of second order mo-
816 ments. *Journal of Geophysical Research: Atmospheres* (1984–2012) 91 (D6),
817 6671–6681.
- 818 Price, J. F., Weller, R. A., Pinkel, R., Jul. 1986. Diurnal Cycling - Observations
819 and Models of the Upper Ocean Response to Diurnal Heating, Cooling, and
820 Wind Mixing. *Journal of Geophysical Research-Oceans* 91 (C7), 8411–8427.
- 821 Ramachandran, S., Tandon, A., Mahadevan, A., 2013. Effect of subgrid-scale
822 mixing on the evolution of forced submesoscale instabilities. *Ocean Modelling*
823 66, 45–63.
- 824 Samelson, R. M., 1993. Linear instability of a mixed-layer front. *J. Geophys.*
825 *Res.* 98 (C6), 10195–10204.
826 URL <http://dx.doi.org/10.1029/93JC00457>
- 827 Sasaki, H., Klein, P., Qiu, B., Sasai, Y., Dec. 2014. Impact of oceanic-scale
828 interactions on the seasonal modulation of ocean dynamics by the atmosphere.
829 *Nat Commun* 5.
830 URL <http://dx.doi.org/10.1038/ncomms6636>
- 831 Shakespeare, C. J., Taylor, J. R., 2013. A generalised mathematical model of
832 geostrophic adjustment and frontogenesis: uniform potential vorticity. *Jour-*
833 *nal of Fluid Mechanics* 736, 366–413.

- 834 Shcherbina, A. Y., D'Asaro, E. A., Lee, C. M., Klymak, J. M., Molemaker, M. J.,
835 McWilliams, J. C., 2013. Statistics of vertical vorticity, divergence, and strain
836 in a developed submesoscale turbulence field. *Geophysical Research Letters*
837 40 (17), 4706–4711.
- 838 Skillingstad, E. D., Samelson, R., 2012. Baroclinic frontal instabilities and tur-
839 bulent mixing in the surface boundary layer. Part I: Unforced simulations.
840 *J.Phys.Oceanogr.* 42 (10), 1701–1716.
- 841 Smagorinsky, J., 1963. General circulation experiments with the primitive equa-
842 tions: I. The basic experiment. *Mon.Weather Rev.* 91 (3), 99–164.
- 843 Spall, M. A., 1997. Baroclinic jets in confluent flow. *J. Phys. Oceanogr.* 27 (6),
844 1054–1071.
- 845 Stone, P. H., 1966. On Non-Geostrophic Baroclinic Stability. *Journal of the*
846 *Atmospheric Sciences* 23 (4), 390–400.
- 847 Sutherland, G., Christensen, K. H., Ward, B., 2014. Evaluating Langmuir tur-
848 bulence parameterizations in the ocean surface boundary layer. *Journal of*
849 *Geophysical Research-Oceans* 119 (3), 1899–1910.
- 850 Tandon, A., Garrett, C., Jun. 1994. Mixed-Layer Restratification due to a Hori-
851 zontal Density Gradient. *Journal of Physical Oceanography* 24 (6), 1419–1424.
- 852 Taylor, J. R., Ferrari, R., Jun. 2010. Buoyancy and Wind-Driven Convection at
853 Mixed Layer Density Fronts. *Journal of Physical Oceanography* 40 (6), 1222–
854 1242.
855 URL <http://journals.ametsoc.org/doi/abs/10.1175/2010JP04365.1>
- 856 Thomas, L., Ferrari, R., Nov. 2008. Friction, Frontogenesis, and the Stratifica-
857 tion of the Surface Mixed Layer. *Journal of Physical Oceanography* 38 (11),
858 2501–2518.
859 URL <http://journals.ametsoc.org/doi/abs/10.1175/2008JP03797.1>
- 860 Thomas, L. N., 2005. Destruction of potential vorticity by winds. *Journal of*
861 *Physical Oceanography* 35 (12), 2457–2466.
- 862 Thomas, L. N., Sep. 2012. On the effects of frontogenetic strain on symmetric
863 instability and inertia-gravity waves. *Journal of Fluid Mechanics* 711,
864 620–640.
865 URL http://www.journals.cambridge.org/abstract_S0022112012004168
- 866 Thomas, L. N., Taylor, J. R., Sep. 2010. Reduction of the usable wind-work on
867 the general circulation by forced symmetric instability. *Geophysical Research*
868 *Letters* 37 (18).
869 URL <http://doi.wiley.com/10.1029/2010GL044680>

- 870 Thomas, L. N., Taylor, J. R., Ferrari, R., Joyce, T. M., Jul. 2013. Symmetric
871 instability in the Gulf Stream. *Deep Sea Research Part II: Topical Studies in*
872 *Oceanography* 91, 96–110.
873 URL <http://linkinghub.elsevier.com/retrieve/pii/S0967064513000829>
- 874 Thomsen, S., Eden, C., Czeschel, L., Nov. 2013. Stability Analysis of the
875 Labrador Current. *J. Phys. Oceanogr.* 44 (2), 445–463.
876 URL <http://dx.doi.org/10.1175/JPO-D-13-0121.1>

ACCEPTED MANUSCRIPT